Natural Hazards
and Earth System
Sciences
Discussions

Topographic controls on landslide mobility: Modeling hurricane-induced landslide runout and debris-flow inundation in Puerto Rico

Dianne L. Brien[1], Mark E. Reid[1], Collin Cronkite-Ratcliff[2], Jonathan P. Perkins[2]

[1]U.S. Geological Survey, Volcano Science Center, Moffett Field, CA, 94035, USA

5 [2]U.S. Geological Survey, Geology, Minerals, Energy, and Geophysics Science Center, Moffett Field, CA, 94035, USA

Correspondence to: Dianne L. Brien (dbrien@usgs.gov)

Abstract. In 2017, Hurricane Maria triggered more than 70,000 landslides in Puerto Rico. After initiation, these predominantly shallow landslides mobilized to varying degrees – some landslides only traveled partway downslope, whereas others reached drainages and mobilized into long-traveled debris flows that could severely impact roads and infrastructure. Thus, forecasting

10 potential landslide runout and inundation zones is critical for estimating landslide and debris flow hazards. Here we conduct an in-depth topographic analysis of landslide-affected areas from nine study areas and apply a linked modeling technique to estimate locations susceptible to varying degrees of landslide runout in Lares, Utuado and Naranjito municipalities.

We find that longer runout length is observed on high-relief escarpments, although highly mobile long-runout debris flows also occurred in lower-relief dissected uplands. These topographic differences indicate that landslides initiating under

15 similar conditions and possessing equal potential to mobilize as debris flows may not travel the same distances or affect the same areal extent. Our modeling approach allows the local topography to automatically control the implementation of two runout methods: 1) *H/L* runout zones are assigned directly downslope of landslide source zones, and 2) debris-flow inundation zones are estimated in the presence of a channel network. Debris-flow volumes are calculated as a function of area-integrated growth factors, estimated as a function of the upstream areas susceptible to shallow landslides. Applying our empirical modeling scheme

20 over an area of 560 km^2, our results highlight the efficacy of our methods for assessment of the potential for landslide runout and debris-flow inundation over diverse terrains with varied susceptibility.

1 Introduction

Globally, 55,997 fatalities due to non-seismically triggered landslides were recorded over the twelve-year period between January 2004 and December 2016 (Froude and Petley, 2018). When conditions for landslide mobilization exist, including at least

25 partial liquefaction by high pore pressures, landslides may mobilize to form debris flows, fast-moving slurries of saturated, poorly sorted sediment (e.g., Iverson, 1997; Hungr et al., 2002). Fast-moving, far-traveled landslides, such as debris flows, are one of the most destructive types of landslides. Due to their rapid velocity and occurrence without warning, debris flows can be lethal (e.g., Highland and Bobrowsky, 2008; McDougall, 2017). In regions where humans and infrastructure are present, landslide susceptibility forecasting tools to identify potential runout zones for high-mobility landslides are of foremost

30 importance.

Landslide susceptibility models typically focus on a single type of landslide or process of movement, either landslide initiation (e.g., Montgomery and Dietrich, 1994; Larsen and Parks, 1998; Pack et al., 1999; Baum et al., 2008; Lepore et al., 2012; Mergili et al., 2014; Reid et al., 2015; Merghadi et al., 2020; Hughes and Schulz, 2020) or runout (e.g., Guzzetti at al., 2006; McDougall, 2017). Runout models may be empirically (e.g., Iverson et al., 1998; Horton et al., 2013; Berti and Simoni,

35 2014) or physics-based (e.g., McDougall and Hungr, 2004; Christen et al., 2010; George and Iverson, 2014; Iverson and George,

2014; FLO-2D Software Inc., 2007; Gorr et al., 2022) and are often focused on back-analysis or site-specific investigations (e.g., McDougall, 2017), typically requiring detailed information about location of landslide initiation and volume or a flow hydrograph (e.g., Barnhart et al., 2021). Empirical runout methods, based on power-law volume/area relations, such as Laharz (Iverson et al., 1998; Schilling, 2014) or DFLOWZ (Berti and Simoni, 2014), provide methods for automated delineation of

40 inundation areas of lahars (e.g., Major et al., 2004; Muñoz-Salinas et al., 2009) or debris flows (Crosta et al., 2002; Griswold and Iverson, 2008; Magirl et al., 2010). Several previous investigations have combined landslide models to estimate both landslide source (initiation) and runout zones. These investigations incorporated empirical models (Guinau et al., 2007; Mergili et al., 2019), physics-based models (Hsu and Liu, 2019), or a combination of empirical and physics-based methods (Ellen et al., 1993; Benda et al., 2007; Bregoli et al., 2010; Park et al., 2016; Fan et al., 2017; Pollock et al., 2019). However, existing methods for

45 analyzing runout do not directly account for location within the topography and the transition from non-channelized to channelized runout.

We build a conceptual framework to define zones of mobility within the landscape that provides the basis of our topographic analysis of landslide-affected areas (source and runout) and modeling approach in Puerto Rico. Landslide materials move downslope until they reach a stable position. Whereas some landslides travel only partway downslope (Fig. 1b), others

50 reach drainages and mobilize into debris flows that can severely impact roads and infrastructure. Non-channelized runout zones exist downslope of landslide source zones, where the source zone is not adjacent to the channel or in open-slope topographies (Fig. 1a). In open-slope topographies, no channels are present and landslides travel downslope without entering a drainage or topographic depression (Geotechnical Engineering Office, 2012). Where channels are present, highly mobile debris flows will travel into the channel, potentially grow in volume, and flow long distances downstream (Fig. 1c). Our empirical runout models

55 allow topography to control the spatial distribution and extent of potential landslide runout and debris-flow inundation zones. Our approach simulates patterns consistent with observations from Hurricane Maria when applied over a topographically diverse area, including the full extent of three municipalities: Lares, Utuado and Naranjito. Our USGS software package, Grfin Tools (Cronkite-Ratcliff et al., in review; Reid et al., in review) implements these methods and enables runout assessment over large regions without the computational effort required by physics-based models.

Natural Hazards
and Earth System
Sciences

Open Access

EGU

Discussions
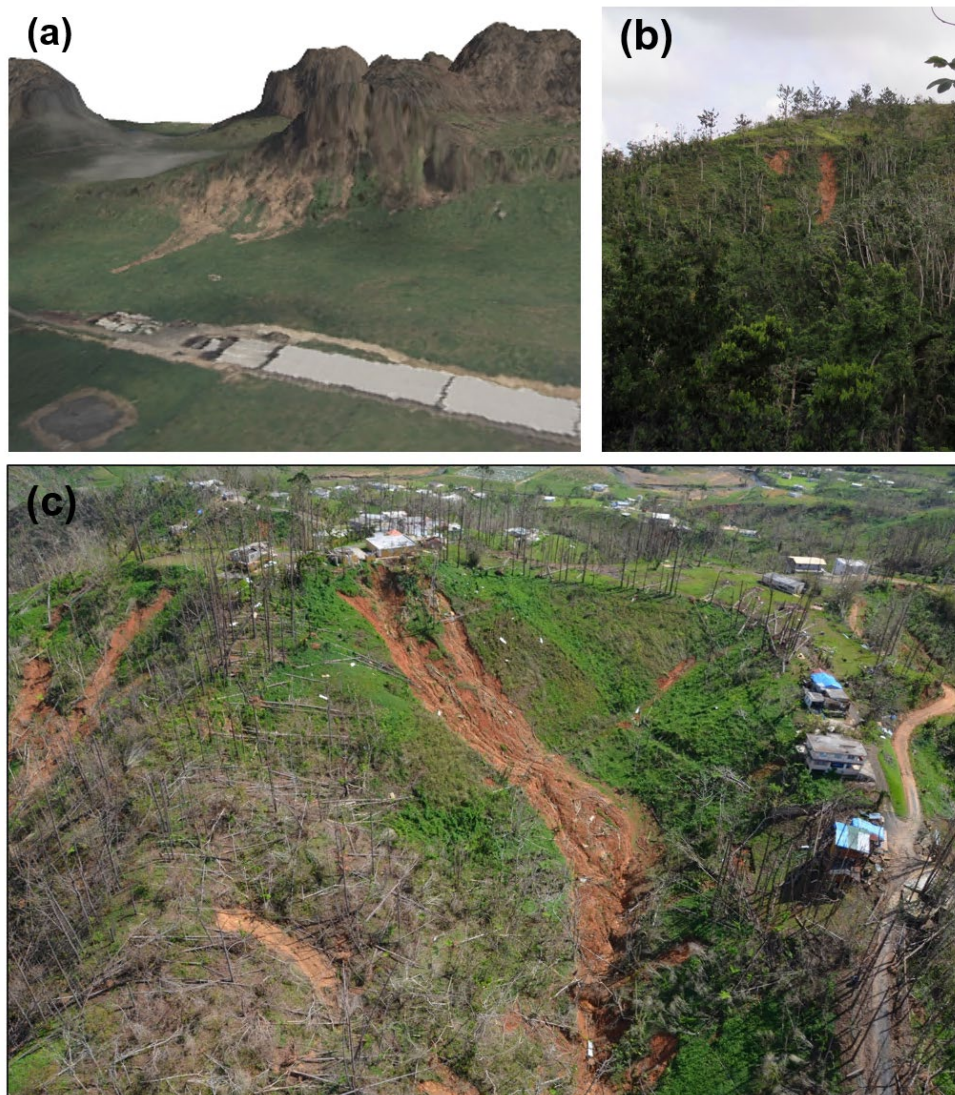
Figure 1. Photographs showing Hurricane Maria landslides with varied levels of mobility a) Orthophoto (Quantum Spatial 2017) draped on DEM (U.S. Geological Survey 2020), showing multiple landslides in non-channelized, open-slope topography of northern Utuado, adjacent to a cone karst topography. b) Photograph of two moderate-mobility, shallow landslides, in Utuado, Puerto Rico, that mobilized and travelled partway downslope but insufficient distance to reach a channel. c) Photograph of higher-mobility debris flow that initiated from multiple shallow landslides and entered channelized topography in the lower half of photo, in the Ciales municipality, Puerto Rico. Photograph in c by Jason Kean (USGS).

Natural Hazards
and Earth System
Sciences
Discussions

2 Conceptual framework

2.1 Zones of mobility

70 Our conceptual framework uses three zones of mobility within the landscape: 1) source zones, 2) non-channelized runout zones, and 3) channelized runout zones (debris-flow inundation zones). This framework provides the foundation to investigate two interrelated aspects of the Hurricane Maria landslides: 1) a topographic analysis of published landslide inventories and 2) a modeling approach to assess susceptibility to non-channelized and channelized runout in Puerto Rico. Results of the topographic analysis inform our selection of model parameters for candidate susceptibility scenarios, with the overall objective to select two final scenarios for regional susceptibility maps.

2.2 Topographic analysis

75

Our topographic analysis guided the selection of input parameters for runout modeling and provided a complementary analysis associated with zones of mobility, enabling us to gain perspectives on the landslide-affected areas and relative contributions of each zone of mobility. Published landslide inventories of Hurricane Maria landslides (Bessette-Kirton et al., 2019b; Baxstrom et al., 2021a, 2021b; Einbund et al., 2021a, 2021b) provided the location of landslide-affected areas for our topographic analysis, 80 whereby we analyzed the percentage of area affected by each zone of mobility for Hurricane Maria landslides and extracted slope characteristics within each zone. We also assessed correlations between study area slope and the slope of source areas and non-channelized runout, as trends could influence whether different parameters are needed for runout modeling as a function of geologic or topographic variability. In addition, we identified a subset of the mapped landslides, representative of the most mobile channelized debris flows. Typical characteristics of the inundation zones associated with the most mobile debris flows 85 allowed us to define parameters for potential zones of debris-flow growth in our debris-flow inundation modeling. These inundation zones provided an important component for assessment of the predictive success of our inundation methods.

2.2 Linked-model approach

We developed a linked-model approach that combines landslide source with two methods to identify areas susceptible to landslide runout and debris-flow inundation. Here, the "link" is joined independently between potential landslide source areas 90 and each runout method (Fig. 2).

The runout methods differ based on the relative mobility and topographic setting of landslides. For moderate mobility landslides and/or non-channelized runout zones, we define potential runout zones by minimum angle of reach (arctan(height/length)) from the landslide source. This approach provides a methodology to 1) estimate runout in open-slope topographies where channels are not present, and 2) provide a transition from upslope landslide source zones to channels.
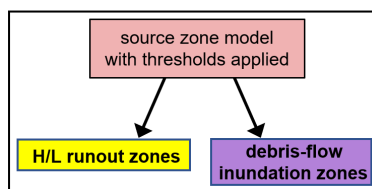
95

Figure 2. Schematic of linked-model approach.

Natural Hazards
and Earth System
Sciences
Discussions

Although other types of landslides may flow, the definition of debris flow provided by Hungr et al. (2014) is well aligned with our modeling approach for inundation zones: "Very rapid to extremely rapid surging flow of saturated debris in a steep channel. Strong entrainment of material and water from the flow path". These debris flows can increase in volume as they travel, due to a combination of processes, including entrainment of bed sediment (e.g., Hungr et al., 1984; Takahashi, 1991; Iverson et al., 2011), coalescence of landslides (e.g., Coe et al., 2021), and stream bank collapse (Johnson, 1970). For channelized debris flows, we identify potential inundation zones using empirical volume-area relations (Griswold and Iverson, 2008) in concert with empirical debris-flow growth factors (Reid et al., 2016). Our growth factors integrate growth over a drainage basin and are defined as a function of upstream contributing area susceptible to shallow landslides. This approach determines the spatial distribution and volumes of runout material contributing to debris-flow inundation zones.

Our linked-model approach 1) provides three zones of hazard (landslide source, non-channelized runout, and channelized runout) related to landslide mobility, 2) uses angle of reach to identify potential non-channelized runout zones, 3) incorporates debris-flow growth for channelized debris flows, 4) estimates debris-flow volumes as a function of contributing area susceptible to landslides, and 5) applies volume-area relations to estimate corresponding areas of debris-flow inundation. Combined, this approach provides a GIS-based method, applicable over diverse terrains of varied susceptibility to debris flows. Our USGS software package, Grfin (gr=growth + f=flow + in=inundation; pronounced griffin) Tools (Cronkite-Ratcliff et al., in review; Reid et al., in review) implements this approach and enables runout assessment over large regions without the computational effort typically required by physics-based models. We used our linked-model approach to create regional susceptibility maps of landslide initiation and runout in the three municipalities of Lares, Utuado and Naranjito, Puerto Rico.

3 Study areas

Steep mountainous terrain, high mean annual rainfall, and frequent intense storms in Puerto Rico contribute to the frequent occurrence of landslides, resulting in extensive property damage and loss of life (e.g., Larsen and Torres-Sanchez, 1998). Rainfall-triggered landslides are the most common type of landslide, occurring throughout the central mountains and foothills of the island, as frequently as 1 to 2 times per year (Larsen and Simon, 1993). On 20 September 2017, Hurricane Maria produced rainfall amounts greater than any other hurricane or tropical storm in Puerto Rico since 1956; within a 48-hour period, at least 250 mm of rain fell across Puerto Rico's mountainous terrain (e.g., Bessette-Kirton et al., 2019a) with as much as 1029 mm of precipitation recorded in the southeastern part of the island (Keellings and Hernández Ayala, 2019). Hurricane Maria triggered more than 70,000 landslides in Puerto Rico (Hughes et al., 2019). Our work builds on published data sources related to the widespread landsliding that occurred during Hurricane Maria.

3.1 Data sources and related work

3.1.1 Topographic base

We used high-resolution pre- and post- Hurricane Maria lidar-derived DEMs to construct a channel network and determine flow directions for our runout modeling. A pre-Maria, 1 m resolution DEM, acquired between January 2016 and March 2017 (U.S. Geological Survey, 2018) was representative of the topography at the time of Hurricane Maria. This pre-Maria DEM was used for extraction of topographic characteristics and assessment of model predictive success. A 0.5 m resolution, post-Maria lidar-derived DEM (U.S. Geological Survey, 2020a,b,c) was resampled to 1 m and used to create regional susceptibility maps of landslide initiation and runout.
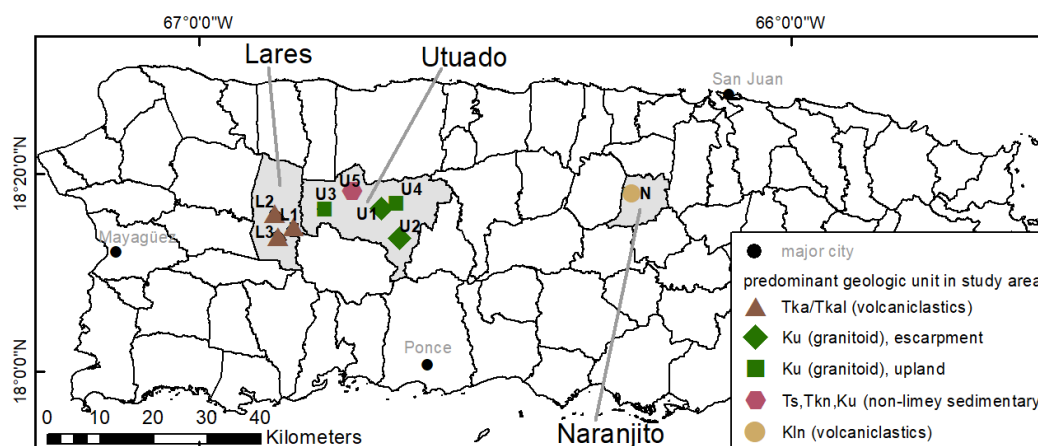
3.1.2 Mapped landslide inventories

Published landslide inventories (Bessette-Kirton et al., 2019b; Baxstrom et al., 2021a, 2021b; Einbund et al., 2021a, 2021b)
135   provided detailed mapping of landslide-affected areas from Hurricane Maria, including 2919 locations of landslide headscarp points, travel distance lines, landslide-affected areas, and source-area-only locations. Lengths were measured from the top of the headscarp to the farthest extent of visible landslide deposits (Bessette-Kirton et al., 2020). Hurricane Maria source-area locations were determined from pre- and post-event lidar-derived DEM differences (2016 to 2018) (U.S. Geological Survey, 2018, 2020a,b,c).

140   The inventories encompassed nine study areas, within three municipalities, over four distinctive geologic terranes — defined as groups of geologic formations, based on lithologic rock type, depositional environment, and/or age (Bawiec, 1998) (Table 1). Based on municipality, we applied naming conventions to identify the study areas. The Utuado municipality includes four ~2.5 km^2 study areas (U1, U2, U3, U4, Fig. 3) in a granitoid terrane (Ku) consisting of the Utuado batholith; these four areas are further distinguished by two geomorphic terrains (Einbund et al., 2021b): 1) escarpments (U1, U2) having highly dissected
145   areas with predominantly steep topography and high drainage density and 2) upland terrain (U3, U4) consisting of dissected, low-relief plateaus (Monroe, 1980) with lower drainage density, relative to escarpments. Study areas U5, L1, L2, L3, and N (Fig. 3) do not have a distinctive plateau expression and do not contain a single unique geomorphic terrain. Northern Utuado includes the largest (~30 km^2) study area (U5), with low landslide density, located in non-limey sedimentary units (Baxstrom et al., 2021b) adjacent to cone-karst topography, where conical, steep-sided hills of the Lares Limestone, named mogotes, rise to
150   heights up to 100 m (Monroe, 1976). The Lares municipality includes three ~3.5 km^2 study areas (L1, L2, L3) (Einbund et al., 2021a), located in Tertiary-Cretaceous marine volcaniclastics, consisting mainly of breccia, tuff, sandstone, and siltstone (Tka/Tkal). Naranjito municipality contains one ~2.5 km^2 study area (N) (Bessette-Kirton et al., 2019b; Baxstrom et al., 2021a), located in Cretaceous marine volcaniclastics, consisting mainly of basaltic breccia, sandstone, and siltstone (Kln).

155   **Figure 3. Map of Puerto Rico, showing locations of nine study areas with detailed landslide mapping of 2919 landslides in the Lares, Utuado, and Naranjito municipalities (Bessette-Kirton et al., 2019b; Baxstrom et al., 2021a, 2021b; Einbund et al., 2021a, 2021b). Study-area name is indicated by the first letter of the municipality, followed by a numeral.**

Table 2. Study area names, geologic terrane, predominant geologic units (Bawiec, 1998), and geomorphic terrains (escarpment or upland) for nine areas with mapped landslide-affected areas (Bessette-Kirton et al., 2019b; Baxstrom et al., 2021a, 2021b; Einbund et al., 2021a,
160   **2021b). Color and symbol combinations indicate geologic terrane; within the granodiorite. Two unique symbols are used to distinguish escarpment (green diamonds) versus upland (green squares) geomorphic terrains.**

Natural Hazards
and Earth System
Sciences

Open Access

Discussions

EGU

symbol	study area name	geologic terrane	predominant geologic units	geomorphic terrain
◆	U1	granitoid	Ku (Utuado batholith)	escarpment
◆	U2	granitoid	Ku	escarpment
■	U3	granitoid	Ku	upland
■	U4	granitoid	Ku	upland
⬢	U5	non-limey sedimentary	Ts (San Sebastian Formation), Tkn (Naranjito Formation)	not distinguished
▲	L1	marine volcaniclastic	Tka (Anon Formation), Tkal (Anon and Lago Garzas Formations)	not distinguished
▲	L2	marine volcaniclastic	Tka, Tkal	not distinguished
▲	L3	marine volcaniclastic	Tka, Tkal	not distinguished
●	N	marine volcaniclastic	Kln (Los Negros Formation)	not distinguished

3.1.3 Landslide types

Landslides triggered by Hurricane Maria included slumps, debris flows, rockfalls, and other slope failures (Hughes et al., 2019).

165 Most the landslides were shallow debris slides and many of these mobilized and/or coalesced into channelized debris flows (Bessette-Kirton et al., 2020; Coe et al., 2021). Figure 4 shows the variety of landslide styles associated with channelized (Fig. 4b) and non-channelized (Fig. 4a) topography. In adjacent drainages, landslide density and the mobility of these landslides can be widely varied (Fig. 4b).
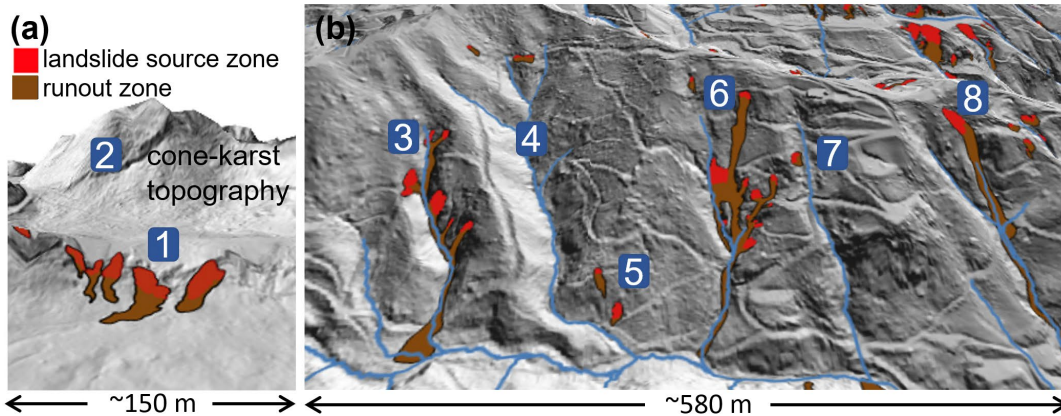
170

Figure 4. Perspective views showing topographic features, mapped landslide source areas, and runout in small sections of two study areas. a) Landslides on non-channelized open-slope terrain (1) in Northern Utuado (study area U5) (Baxstrom et al., 2021b), adjacent to cone-karst topography (2). b) Study area N (Bessette-Kirton et al., 2019b; Baxstrom et al., 2021a), showing basins with varying landslide density and landslide types: 3. basin affected by landslides coalescing into debris flows, 4. unaffected basin, 5. low mobility

175 landslides on cut-slopes adjacent to roads, 6. landslide on hillslope coalescing with multiple landslides closer to or located in drainage, 7. basin with one-small, low mobility landslide, and 8. a single landslide near the top of the hillslope that mobilized as a channelized debris flow. Approximate location of a at center of image is 18° 18′ 10″ N, 66° 49′ 10″; b is located at 18° 18 ′0″ N, 66° 16′ 0″ W.

Natural Hazards
and Earth System
Sciences

Open Access

EGU

Discussions

3.1.4 Potential landslide source areas

180 To estimate potential landslide source areas in our linked-model approach, we used areas identified from the combination of soil-depth estimations, pore-water pressures, and slope stability analysis. The areas susceptible to shallow landslides during prolonged, intense rainfall were defined by factor of safety thresholds for high and very high susceptibility scenarios. Details of the source area modeling are provided in Baum et al. (2024).

3.1.5 Debris-flow growth and volumes

For our debris-flow inundation modeling, we used published estimates of debris-flow growth factors and volumes. These
185 estimates (Table 2) were based on lidar-derived DEM differencing in four drainage basins affected by long-runout debris flows from Hurricane Maria (Coe et al., 2021). Growth factors based on upslope contributing areas are shown as a function of both i) full contributing area and ii) area susceptible to landslides, approximated as slopes greater than 30° (Coe et al., 2021), where i is applicable to basins of similar susceptibility and ii is applicable to regions with spatially variable landslide susceptibility patterns.

Field measurements of stream slopes for several Hurricane Maria debris flows were measured using a laser rangefinder
190 with inclinometer (Coe et al., 2021). These measurements showed that growth transitioned to deposition at a stream slope between 3 to 8°, providing constraints on debris-flow growth zones for our modeling.

Table 2. Range of values for debris-flow growth factors and total volumes from Hurricane Maria debris flows (Coe et al., 2021).

	range of values
i) area-based growth factors, full contributing area (c_1)	0.01–0.13 $m^3\,m^{-2}$
ii) area-based growth factors (c_1), calculated as the percentage of area with slopes > 30°	0.02–0.21 $m^3\,m^{-2}$
iv) total volumes (V)	840–12,770 m^3

4 Methods

195 Figure 5 shows a flowchart illustrating the methods for our topographic analysis and linked-model approach, where blue boxes and one red box indicate existing data sources. The left side the flow chart (gray) shows our workflow for topographic analysis and the right side (tan) shows the steps for our linked-model approach. The three components of the linked-model are shown: 1) source (red), 2) non-channelized runout (yellow), and 3) debris-flow inundation (purple).

Natural Hazards
and Earth System
Sciences

Open Access

EGU

Discussions
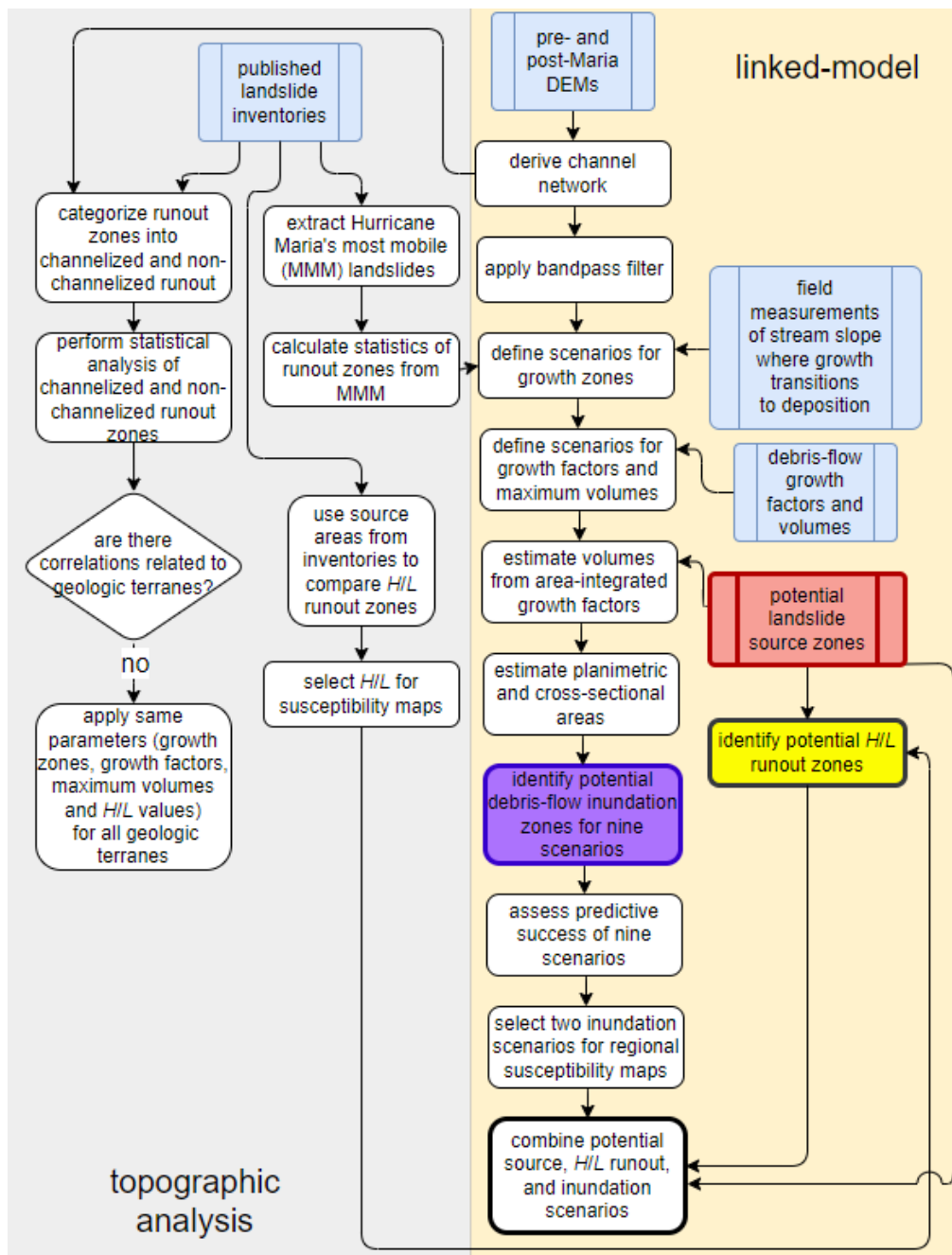
Figure 5. Flowchart of our topographic analysis and linked-model approach. Blue boxes (and one red box) indicate published data sources. Red, yellow, and purple boxes indicate the three components of our linked-model approach.

4.1 Channel network delineation

Delineation of a channel network derived from the 1 m DEMs was essential for derivation of flow direction and flow accumulation for runout modeling, as well as the distinction of non-channelized versus channelized runout zones. Roads are an

Natural Hazards
and Earth System
Sciences
Discussions

205   inherent problem for channel detection algorithms that use high-resolution topographic data, as roads often obscure the topography of natural channels. In Puerto Rico, large municipal roads, along with small agricultural and private roads (Ramos-Scharrón et al., 2021), led to significant disruption of the flow directions derived from the DEMs. Whereas some debris flows from Hurricane Maria were diverted by these agricultural roads, the majority bypassed roads and continued down natural channels (Bessette-Kirton et al., 2019a). Accurately modeling debris-flow inundation required defining downstream channel

210   networks that were continuous across laterally intersecting road networks.

Our automated methods applied two strategies to eliminate road-network artifacts from the lidar-derived DEMs and construct channel networks representative of natural channels from the lidar-derived DEM: 1) identification of the location of channel initiation using a curvature-based flow accumulation threshold, and 2) spectral filtering of the DEMs to remove road artifacts downstream of channel initiation.

215   **4.1.1 Curvature-based method to identify channel initiation**

Our implementation of curvature-based network delineation was inspired by Tarboton and Ames (2001) and used a flow accumulation threshold including only topographic concavities (hollows) that are representative locations of channel initiation. To detect channel initiation points for our drainage network, we used concave planform curvature to identify areas representative of topographic hollows.

220   Steps in our method to identify locations of channel initiation included: 1) using a local mean to smooth the DEM, 2) calculating planform curvature, 3) applying a curvature threshold to identify concavities in the topography, 4) eliminating small, isolated concavities, 5) calculating the contributing area of remaining concavities, and 6) applying an area threshold using only the contributing area of concave topography. We used threshold values based on topographic scaling factors and published values (Pelletier, 2013; Mudd et al., 2019). The location of channel initiation was assigned where the contributing concave area,

225   defined as a planform curvature < 0.02 m^{-1}, was larger than 500 m^2.

4.1.2 Bandpass DEM to derive flow directions

In areas downstream of channel initiation, the channel network and associated flow directions from the lidar-derived DEMs were sometimes diverted at road intersections. We employed a spectral filtering approach to remove small roads from the topography. Using SpecFiltTools software (Perron et al., 2008), we applied a Gaussian bandpass filter to remove topographic features at the

230   wavelength of small agricultural roads (~10 m) while retaining both the smaller and larger wavelengths that constitute the undisturbed topography. The combination of our two strategies provided an automated method to remove roads from channel networks over diverse geomorphic and geologic terranes.

4.2 Topographic analysis of mobility zones

Using the published datasets of source areas and landslide-affected areas (Bessette-Kirton et al., 2019b; Baxstrom et al., 2021a, 2021b; Einbund et al., 2021a, 2021b), combined with our channel network, we divided the mapped landslide-affected areas in

235   the nine study areas into the three zones of mobility. The published mapped source areas provided the first zone of mobility. Using ArcGIS® spatial analyst tools by Esri, we divided the remaining area into non-channelized and channelized runout. Runout zones from small landslides (length < 20 m) with a small percentage (< 20%) of area adjacent to the drainage or distanced greater than 3 m from the delineated drainage network were assigned as non-channelized runout and the remaining

240   area was designated as channelized runout.

Within the three mobility zones, we: 1) evaluated the percentage of each study area affected by each zone, 2) analyzed summary statistics to compare the distribution of topographic slopes in the three mobility zones, and 3) compared variability between study areas. Summary statistics were analyzed based on every raster cell within a mobility zone.

To evaluate the percentage of each study area affected by landslide source zones, we considered: 1) percentage of full study area, and 2) percentage of each study area susceptible to landslides, approximated by steep slopes greater than 30° (Coe et al., 2021). This approximation of susceptible areas was consistent with field observations of Baum et al. (2018), and provides a justifiable criterion to calculate normalized values, whereby, the percentage of area affected would be equal across all study areas if all other contributing factors were equal.

Summary statistics, for each mobility zone in each study area, included percentiles and the Fisher-Pearson coefficient of skewness (G_1) (Zwillinger and Kokoska, 2000), a measure of the asymmetry of a statistical distribution, where $-0.5 < G_1 < 0.5$ indicates the data are approximately symmetric; $-1 < G_1 < -0.5$ indicates the data are moderately left-skewed; $0.5 < G_1 < 1$ indicates the data are moderately right-skewed; $G_1 < -1$ indicates the data are highly left-skewed; $G_1 > 1$ indicates the data are highly right-skewed (Brown, 2022).

4.2.1 Hurricane Maria's most mobile (MMM) landslides

Next, we developed criteria to extract a subset of mapped landslide-affected areas representative of Hurricane Maria's most mobile channelized debris flows (MMM). The identification of MMM provided a dataset for assessment of predictive success of our debris-flow inundation modeling. Characterization of the runout zones associated with the MMM debris flows guided the parameterization of debris-flow growth zones.

The primary criterion to identify MMM was a high (> 40%) percentage of runout area located in close proximity (< 5 m) to a designated channel. This criterion identified channelized debris flows as well as some less mobile, non-channelized runout zones located close to the channel. To eliminate these non-channelized runout zones, we applied an additional criterion, runout length >100 m. We used runout lengths available in the published landslide inventories. Given that post-event evidence did not provide information to distinguish specific contributions from sources upstream of tributary junctions, coalescing runout zones were grouped together; one runout zone may represent the path of a single debris flow or many coalescing debris flows. We applied these two criteria to extract MMM for the nine study areas (Brien et al., in press).

To evaluate representative characteristics of channelized debris-flow runout zones and define constraints on debris-flow growth zones for inundation modeling, we compiled percentile statistics from the runout zones associated with MMM. These zones may have included stream reaches of growth, transport and/or deposition. We were not able to identify reaches with only debris-flow growth given the available information, therefore the values extracted represent extremes of reasonable values to constrain debris-flow growth zones. Due to the small sample size for upland terrains for this analysis, we grouped the study areas by geologic terrane.

We computed percentile statistics within the runout zones, where the maximum value of stream order provided the most useful statistic to constrain characteristics of growth zones and other variables described below were characterized by means. For each runout zone, we determined the maximum Strahler stream order, mean stream slope calculated over a horizontal distance of 50 m, mean planform curvature from a smoothed DEM, and mean percentage of contributing area susceptible to shallow landslides (P_{src}), where:

$$P_{src} = 100 \left(\frac{A_{src}}{A} \right) \tag{1}$$

A_{src} is total contributing area susceptible to shallow landslides, estimated from source-zone modeling (Baum et al., 2024) and A is total contributing area. Contributing areas and corresponding values for P_{src} were calculated for each raster cell within a runout

280 zone using a single direction *D-8* flow model (Tarboton et al., 2015).

4.3 Linked-model approach

4.3.1 Landslide initiation zones

Potential source areas for our runout methods can be obtained from any empirical- (e.g., Furbish and Rice, 1983; Larsen and Parks, 1998; Lepore et al., 2012; Hughes and Schulz, 2020; Merghadi et al., 2020) or physics-based (e.g., Montgomery and

285 Dietrich, 1994; Pack et al., 1999; Baum et al., 2008; Mergili et al., 2014; Reid et al., 2015) landslide susceptibility methods. For Puerto Rico, we used slope stability analysis results to identify potential source areas. Baum et al. (2024) defined factor of safety thresholds needed to capture 0.75 (high susceptibility) and 0.90 (moderate susceptibility) true positive rate for observed headscarp points (from Hughes et al., 2019) of landslides triggered by Hurricane Maria. For our non-channelized runout zones, discussed below, we used the combined high and moderate susceptibility potential source areas. The high-susceptibility areas

290 were used as the upslope contributing source area for debris-flow inundation scenarios.

4.3.2 Delineation of non-channelized runout zones

We identified runout zones for moderate mobility landslides using *H/L* runout zones delineated with the avalanche runout tool from TauDEM toolbox (Tarboton et al., 2015). This tool uses a *D-infinity* method to determine flow directions along a flow path (Tarboton, 1997). Length downslope of potential source areas is limited by a threshold angle equivalent to arctan (*H/L*) or the

295 angle of reach (α) (e.g., Scheidegger, 1973; Hsu, 1975; Nicoletti and Sorriso-Valvo, 1991; Corominas, 1996; Iverson et al., 2015; Legros, 2002; Wallace et al., 2022), where *H* is defined as the vertical drop, and *L* is the horizontal projection of distance. On a hillslope or in a DEM, the flow path for measurement of the horizontal length, *L* may follow a winding pathway downslope and down-channel. In locations where runout enters a channel, the runout zones defined by *H/L* are not able to delineate width of inundation. This limitation of *H/L* runout estimates is addressed by our application of debris-flow inundation modeling in

300 channelized topography.

4.3.3 Delineation of channelized debris-flow inundation zones

For high mobility, channelized debris flows that grow as they travel, we identified zones of potential debris-flow growth, calculated debris-flow volumes using debris-flow growth factors (Reid et al., 2016) and identified areas susceptible to inundation with Grfin Tools debris-flow inundation model (Cronkite-Ratcliff et al., in review; Reid et al., in review). The Grfin Tools

305 implementation eliminates spiky artifacts that can be present in results using other empirical debris-flow inundation models such as Laharz (Schilling, 2014) or DFLOWZ (Berti and Simoni, 2014).

Our modeling used a semiempirical approach relating volume with cross-sectional and planimetric area (Iverson et al., 1998), allowing us to estimate inundation area from debris flows. This approach uses power-law relations for debris-flow inundation (Griswold and Iverson, 2008) combined with empirical growth factors (Reid et al., 2016; Coe et al., 2021).

310 Planimetric and cross-sectional inundation area estimations are calculated from two statistically derived equations, based on a worldwide database of debris-flow measurements from diverse data sources and geographic locations, ranging in volume from 10 to 10^6 m³ (Griswold and Iverson, 2008):

$$A = 0.1\,V^{2/3} \tag{2}$$

Natural Hazards
and Earth System
Sciences

Discussions

$$B = 20\,V^{2/3} \tag{3}$$

315

where A is cross-sectional area, B is planimetric area, and V is debris-flow volume. Previous studies of non-post-wildfire debris flows yield similar coefficients for these relations, where the cross-sectional area coefficient ranged from 0.07 to 0.1 and the planimetric area coefficient ranged from 17 to 20 (Griswold and Iverson, 2008; Berti and Simoni, 2014). The estimated cross-sectional area and planimetric areas are applied to a DEM to define areas susceptible to channelized debris flows.

320   Debris-flow volume is of foremost importance for this approach and for inundation modeling in general. Previous studies indicate debris-flow inundation patterns and flow depth estimates may be more sensitive to flow volume than flow properties (Barnhart et al., 2021). We compute volume as a function of upslope contributing area susceptible to shallow landslides at locations in the digitally derived channel network where debris-flow growth is likely to occur (growth zones):

$$V = \begin{cases} c_1\,A_{src} & if\ \ c_1\,A_{src} < V_{max} \\ V_{max} & if\ \ c_1\,A_{src} \geq V_{max} \end{cases} \tag{4}$$

325   where V is debris-flow volume, c_1 (units of $L^3\,L^{-2}$) is an empirically derived growth factor (Reid et al. 2016), A_{src} is potential upslope contributing source area, and V_{max} is maximum volume. Volumes are ultimately constrained by V_{max}, based on volumes estimates from Hurricane Maria. Using volumes from Eq. (4), cross-sectional and planimetric inundation areas can be derived using Eqs. (2, 3).

        For Puerto Rico, volumes calculated as a function of areas susceptible to debris flows (A_{src}), based on Baum et al.
330   (2024), allow us to apply these empirical relations over large regions with varied geologic terranes and geomorphic terrains where landslide susceptibility is spatially variable. Equation 4 provides volumes regulated by c_1 and A_{src}. Basins with minimal susceptible area result in smaller volumes and basins of high susceptibility produce larger volumes, limited by V_{max}. For areas with no susceptible contributing source area, debris-flow volumes are nil, and no inundation will be estimated. We use the term "self-regulating" volumes to describe volumes estimated by Eq. (4).

335   **4.4 Parameters and assessment of linked-model approach**

4.4.1 Selection of height/length (H/L) values for regional susceptibility maps

To select H/L values for regional susceptibility maps, we considered a range of previously published H/L values in Puerto Rico as well as global datasets. In Puerto Rico, Bessette-Kirton et al. (2020) calculated median H/L values for 1035 landslides from Hurricane Maria as 0.68 ($\alpha = 34°$) and coalescing landslides as 0.52 ($\alpha = 27°$), with median lengths (L) of 17.5 m and 25.2 m,
340   respectively. These values represent typical Maria-induced landslides with relatively short travel distance, as reflected by the median lengths. The most mobile landslides had H/L values less than 0.25 ($\alpha = 14°$, Bessette-Kirton et al., 2020).

        Other published H/L data for landslides in the volume range from Hurricane Maria include regression equations quantifying the relation between the angle of reach (α) and landslide volume; for all landslide types combined, $\log(H/L) = -0.085\log V - 0.047$ which yields H/L values of 0.61 ($\alpha = 31°$) to 0.41 ($\alpha = 22°$) for landslide volumes of 100 to 10,000 m^3
345   respectively (Corominas, 1996). Data from flume experiments yields $L/H = \sim2$ (equivalent to $\alpha = \sim27°$) for unconfined runout but greater than 2 for channelized runout, for volumes of $\sim10\ m^3$ (Iverson, 1997). Given the wide range of published values, we used mapped landslide source areas to assess the change in area affected by H/L runout over a wide range of α values: 10, 15, 20, 25 and 30°.

4.4.2 Debris-flow growth zones and volumes

350   Debris-flow volumes (Eq. (4)), calculated as a function of upslope contributing area susceptible to shallow landslides, were computed where debris-flow growth is likely to occur. Debris-flow growth zones were defined by a combination of parameters, including stream slope, stream order, planform curvature, and P_{src} (Eq. (1)). The rate of growth was controlled by c_1, limited by V_{max} (Eq. (4)).

            We considered eight debris-flow inundation scenarios (Fig. 6), constrained by 1) the minimum stream slope where
355   growth transitioned to deposition (3°) (Coe et al., 2021), 2) MMM statistics for stream order, stream slope, curvature, and P_{src}, and 3) published debris-flow volumes and growth factors (c_1) (Coe et al., 2021). All scenarios excluded channel sections with planform curvature < 0.02 m^{-1} and $P_{src} < 20\%$, sections unlikely to produce debris-flow growth based on 75–90% of MMM. Unrealistically short (< 4 m) stream segments of channel identified as potential growth zones were also excluded. The final selection of two scenarios for region-wide susceptibility maps was based on evaluation predictive success the inundation results
360   produced from these eight scenarios.

            Columns in the matrix of scenarios (Fig. 6) identify debris-flow growth zone scenarios (A, B, C, D, E). Rows identify associated parameters for debris-flow volumes, including maximum volumes of 1000, 3000, 5000, and 10,000 m^3. Each scenario is assigned an identifier, such as A-1k, based on a combination of the associated letter for growth zone scenario (A) and assigned maximum volume (1k).
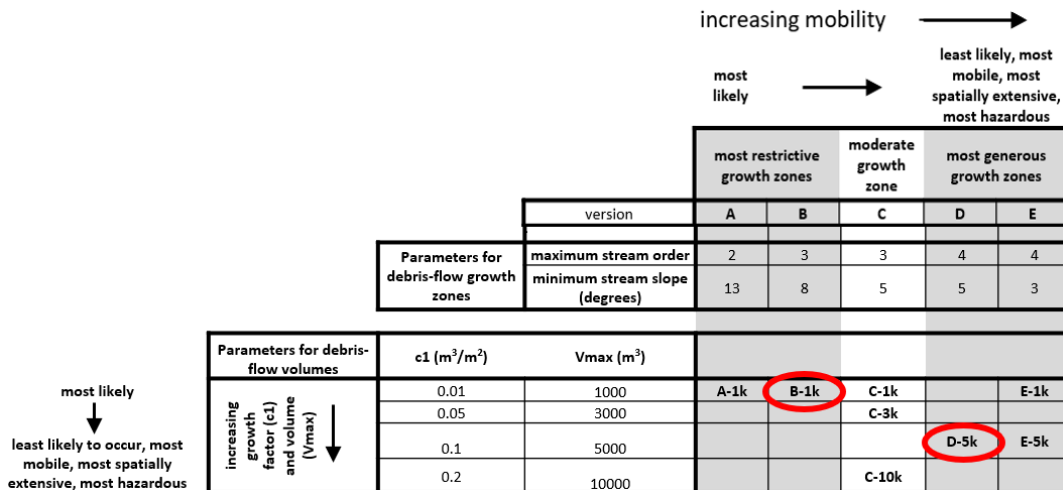
365

Figure 6. Matrix of eight debris-flow inundation scenarios considered in three municipalities. Red outlines highlight two final scenarios selected.

4.4.3 Assessment of predictive success for *H/L*

370   The assessment of predictive success for *H/L* zones was not easily quantifiable given that the landslide inventories were focused on areas with the highest landslide densities. In these high density areas, steep ($> 30°$) slopes led directly to channelized zones and non-channelized runout typically reflected the local topographic slope. In open-slope terrains, a limited number of mapped landslides was represented in the available inventories. We used source areas from the published landslide inventories and considered the spatial patterns in affected areas (non-channelized versus channelized) and increase in estimated runout area for a
375   range of α values between 10 and 30°.

Natural Hazards
and Earth System
Sciences
Discussions

EGU

4.4.4 Assessment of predictive success of debris-flow inundation

In a back-analysis mode commonly used in evaluation of debris-flow runout (McDougall, 2017), we evaluated the success of the eight debris-flow inundation scenarios to predict the presence and extent of 124 debris-flow inundation zones from MMM. Our assessment used contingency table statistics and standard receiver-operator characteristic (ROC) analysis (Powers, 2011) to

380 analyze the predictive success of our results. ROC analysis is based on statistics computed from a binary contingency table, whereby four categories of predictive success are identified: 1) true positive (*TP*) indicates successful prediction of an area susceptible to landslide runout, 2) false positive (*FP*) indicates false prediction of susceptible area, 3) false negative (*FN*) indicates a susceptible area was not identified, and 4) true negative (*TN*) indicates successful prediction of a stable area. We considered three measures of predictive success: 1) true positive rate, $TPR = TP/(TP+FN)$; 2) false positive rate, $FPR =$

385 $FP/(FP+TN)$; and 3) positive likelihood ratio, $PLR = TPR/FPR$.

To select two scenarios for regional susceptibility maps, our ROC analysis used the intersection of 1) inundation zones from Hurricane Maria (MMM) within 5 m of the channel thalweg, and 2) the area encompassed by all inundation scenarios combined. This method evaluated a combination of inundation width and length, but was deleteriously influenced by minor georeferencing discrepancies between the mapped landslides and lidar-derived DEM, as well as underestimation of runout

390 length, where the terminus of debris-flow deposits could not be discerned in the aerial photographs due to uncertainty in debris-flow extent for flows entering drainages where floodwaters reworked deposits (Bessette-Kirton et al., 2019b; Baxstrom et al., 2021a, 2021b; Einbund et al., 2021a, 2021b). For the two selected scenarios, we also assessed TPR to determine success in identification of MMM inundation zones, a method that does not consider runout width or length.

5 Results of topographic analysis

395 **5.1 Zones of mobility**

Figure 7 shows landslide-affected areas (Einbund et al., 2021b), divided into the three zones of mobility: source areas are shown in red, non-channelized runout zones are shown in yellow, and channelized runout zones are shown in purple.
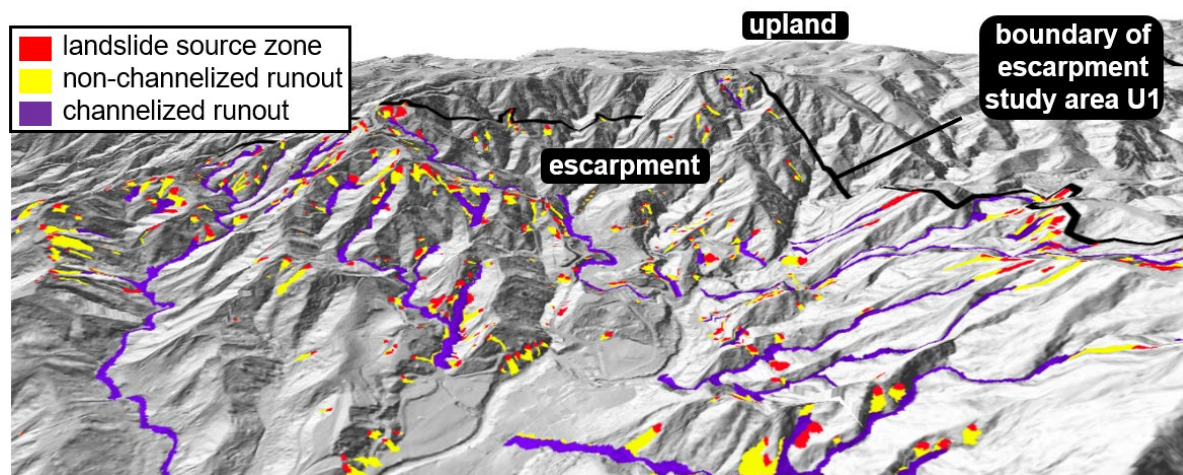

Figure 7. Perspective view showing landslide-affected areas (Einbund et al., 2021b) for study area U1, on an escarpment in the Utuado
400 **municipality, divided into three zones of mobility: 1) source zones (red areas), 2) non-channelized runout (yellow areas), and 3) channelized runout (purple areas). For reference, a dissected upland terrain, representative of topography in U3 and U4, is visible in the background. Approximate location of at center of image is 18° 16′ 40″ N, 66° 41′ 20″ W.**

15

Natural Hazards
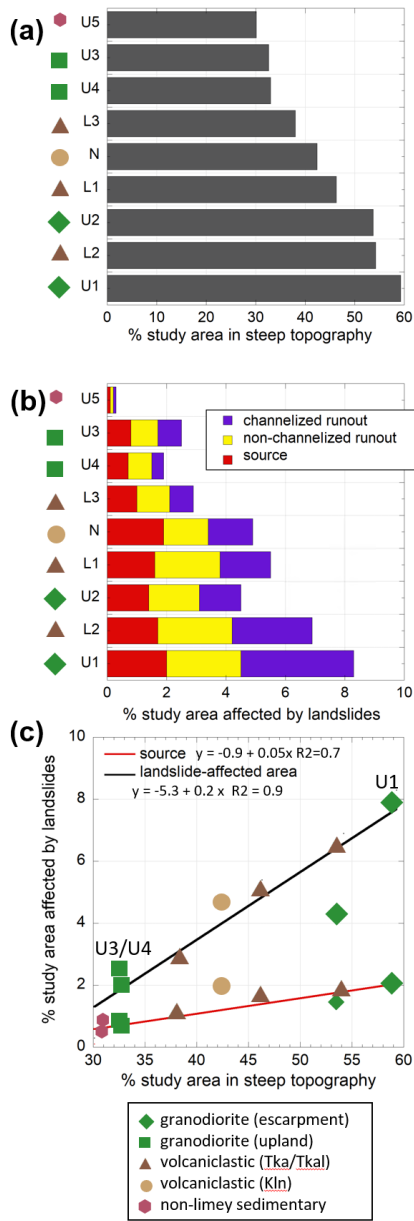and Earth System
Sciences
Discussions
Open Access
EGU

5.2 Area affected by zones of mobility

We assessed the percentage of area affected by each mobility zone in the nine study areas (Table 3). The percentage of the study
405   areas with mapped landslide source zones are shown both as the percentage of study area susceptible to landslides, approximated
as slopes > 30° (column 3), and the percentage of the entire study area (column 4). Although all study areas encompass some
steep topography susceptible to landslides, escarpments (U1, U2) have a majority of the study area susceptible, whereas
dissected uplands (U3, U4) have lower relief and a smaller percentage of the study area in steep ground (Table 3, column 2 and
Fig. 8). Note that the other five study areas (U5, L1, L2, L3, N) contained mixed topography and were not specifically separated
410   into escarpment versus upland terrains.

**Table 3. Percentage of nine study areas susceptible to landslides (column 2) and affected by landslides during Hurricane Maria
(column 7) divided into three zones of mobility: source zone (columns 3 and 4), non-channelized runout (column 5), and channelized
runout (column 6). Column 7 shows the sum of these three zones. The percentage of the study areas with landslide source zones are
shown as the percentage study area susceptible to landslides (column 3) and the percentage of the entire study area (column 4). Study**
415   **areas are listed in order of increasing percentage of area susceptible to landslides (column 2).**

symbol	study area	size (km²) (1)	% study area susceptible to landslides (steep slopes > 30°)		% study area in landslide-affected areas			
			% area with steep slopes (2)	% steep areas with landslide source (3)	% area with source zone (4)	% area with non-channelized runout (5)	% area with channelized runout (6)	% area affected by landslides (total) (7)
●	U5	28.5	30.1%	0.4%	0.1%	0.1%	0.1%	0.3%
■	U3	2.5	32.6%	2.4%	0.8%	0.9%	0.8%	2.6%
■	U4	2.5	33.0%	2.1%	0.7%	0.8%	0.4%	1.9%
▲	L3	3.6	38.0%	2.8%	1.0%	1.1%	0.8%	2.9%
●	N	2.6	42.4%	4.6%	1.9%	1.5%	1.5%	4.9%
▲	L1	3.6	46.3%	3.4%	1.6%	2.2%	1.7%	5.4%
◆	U2	2.5	53.7%	2.7%	1.4%	1.7%	1.4%	4.5%
▲	L2	3.6	54.2%	3.2%	1.7%	2.5%	2.7%	6.9%
◆	U1	2.5	59.3%	3.3%	2.0%	2.5%	3.8%	8.3%

Natural Hazards
and Earth System
Sciences
Discussions

Figure 8. a) Percentage of the nine individual study areas with steep topography. b) Percentage of individual study areas affected by Hurricane Maria landslides, divided into three mobility zones (Table 3). c) Linear regressions of percentage of study area susceptible to shallow landslides (column 2) with percentage of study area affected by 1) source zones (red line; column 4) and 2) total landslide-affected areas (source, non-channelized and channelized runout zones; column 7) (black line). Symbols shown represent geologic terranes and geomorphic terrains of study areas (Fig. 3 and Table 1).

The percentage of each study area affected by landslide source zones (Table 3, column 4) increases slightly with the percentage of the study area susceptible to landslides (column 2). In contrast, the percentage of susceptible area affected by

420

Natural Hazards
and Earth System
Sciences
Discussions

Open Access

EGU

425 landslide sources (column 3) does not consistently increase or decrease. For example, study area N has the median percentage of area susceptible to landslides, but the highest (4.6%) percentage of area affected by landslide sources.

To examine trends in the area affected by landslides for the nine study areas, we fit a linear regression between the percentage of area susceptible to landslides with 1) source zones only and 2) total landslide-affected area. The linear regression produces slopes of 0.05 and 0.2, respectively (Fig. 8c). If all other contributing factors (e.g., rainfall distribution, material

430 properties and hydrologic conditions) were equal, the percentage of susceptible area affected by landslide sources (Table 3, column 3) would be similar across all study areas, whereas the percentage of entire area affected by landslide sources (Table 3, column 4) would increase proportionally to area susceptible to landslides. In addition, if the area affected by landslide runout was directly proportional to the area affected by landslide sources, the slope of the regression lines would be equal. However, in comparison to the relation with source zones only, the percentage of total landslide-affected area increases at a greater rate than

435 the percentage of area with steep slopes. In addition, the ratio between landslide-affected area (Fig. 8c, black line) and landslide source areas only (Fig. 8c, red line) shows the largest difference for study areas with the same underlying geologic terrane (Fig. 8c, U1 and U3/U4), where strength and hydrologic properties would likely be similar.

5.3 Statistical distribution of topographic slopes within mobility zones

We examined the statistical distributions and extracted percentile statistics (P_{10}, P_{25}, P_{50}, P_{75}, and P_{90}) (Fig. 9) for slopes in

440 landslide source zones, non-channelized runout (predominantly runout on hillslopes), and channelized runout zones (Table 4). The median (P_{50}) represents typical slopes of Hurricane Maria landslide-affected areas, whereas P_{10} represents characteristics of higher mobility landslides, with the ability to travel further downstream to areas of more gently sloping topography. Overall, these statistical distributions of slopes for the three zones show a progression of decreasing slopes along the travel path of landslides from Hurricane Maria.

445

Natural Hazards
and Earth System
Sciences
Discussions

Open Access

EGU
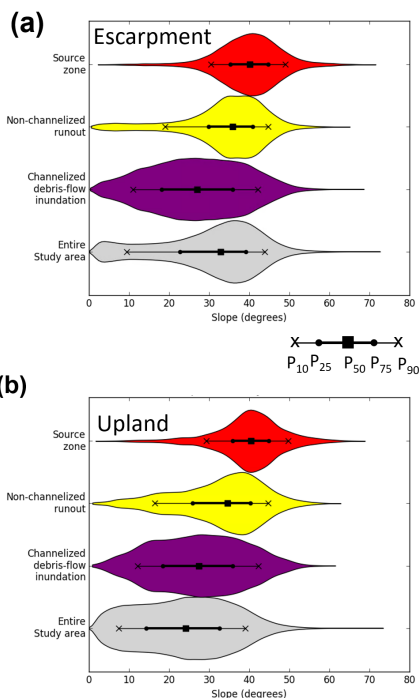
Figure 9. Violin plots showing statistical distribution of slopes in the three zones of landslide mobility and in the entire study area for a) study area U1, a steep escarpment region and b) study area U3, a dissected, upland terrain. Both U1 and U3 are in a granitoid geologic terrane in Utuado. Symbols plotted within the violin plots show the interquartile range (P_{25} to P_{75}), P_{10} and P_{90}

450

Table 4. Percentile statistics of extreme (P_{10}) and average (P_{50}) slopes, in degrees, and the adjusted Fisher-Pearson coefficient of skewness (G_1) (Zwillinger and Kokoska, 2000) for slopes in the entire study areas and mapped landslide-affected areas, divided into the three zones of landslide mobility. The nine study areas are ordered by increasing percentage of area susceptible to landslides. This order also corresponds with the same order as the median slope of the entire study area (column 2).

symbol	study area name	entire study area			source zone			non-channelized runout			channelized runout		
		P_{10} (1)	P_{50} (2)	G_1 (3)	P_{10} (4)	P_{50} (5)	G_1 (6)	P_{10} (7)	P_{50} (8)	G_1 (9)	P_{10} (10)	P_{50} (11)	G_1 (12)
●	U5	4.1	20.7	-0.89	23.1	38.6	0.16	13.4	29.6	-0.59	10.4	23.3	-0.54
■	U3	7.5	24.1	-0.77	29.3	40.4	1.55	16.5	34.5	-0.18	12.2	27.5	-0.73
■	U4	7.7	24.7	-0.61	30.2	40.8	2.12	14.9	31.4	-0.24	11.0	27.5	-0.72
▲	L3	12.1	26.7	-0.41	25.5	36.7	0.72	16.0	29.9	-0.37	13.6	27.8	-0.51
●	N	9.7	27.8	-0.46	25.5	35.6	0.86	12.6	29.6	-0.14	10.1	26.2	-0.71
▲	L1	10.1	28.6	-0.70	29.0	40.0	1.75	21.9	37.5	0.52	17.0	34.1	-0.46
◆	U2	12.5	30.9	-0.18	28.3	37.8	1.39	17.5	32.4	0.62	13.5	29.7	-0.45
▲	L2	11.8	31.4	-0.43	31.6	41.1	2.56	23.8	39.0	1.08	17.9	34.7	-0.47
◆	U1	9.5	32.8	-0.35	30.5	40.2	1.69	19.0	35.8	1.13	11.0	27.0	-0.69

Table 5. Minimum, maximum, mean, and standard deviation of P_{10} and P_{50} in the nine study areas (Table 4) for slopes (in degrees) in the entire study areas and for mapped landslide-affected areas, divided into the three zones of mobility.

	entire study area		source zones		non-channelized runout		channelized runout	
	P_{10} (1)	P_{50} (2)	P_{10} (3)	P_{50} (4)	P_{10} (5)	P_{50} (6)	P_{10} (7)	P_{50} (8)
minimum	4.1	20.7	23.1	35.6	12.6	29.6	10.1	23.3
maximum	12.5	32.8	31.6	41.1	23.8	39.0	17.9	34.7
mean	9.7	27.8	29.0	40.0	16.5	32.4	12.2	27.5
standard deviation (σ)	2.7	3.9	2.8	1.9	3.7	3.6	2.8	3.7

455   Variability between median (P_{50}) source-zone slopes in nine study areas was minimal, ranging from 35.6 to 41.1°, with a standard deviation (σ) of 1.9° (Table 5, column 4). In contrast, median slopes within the study areas, non-channelized and channelized runout zones (Table 4) showed almost twice the variability (σ = 3.9, 3.6, and 3.7°, respectively) (Table 5, columns 2, 6, 8). Extreme (P_{10}) values for study areas, source zones, non-channelized runout, and channelized runout (Table 4) displayed slightly higher variability (σ = 2.7, 2.8, 3.7, and 2.8°, respectively) between study areas (Table 5, columns 1, 3, 5, 7), compared

460   to P_{50} of source-zones.

We quantified the asymmetry of the statistical distributions, using skewness (G_1) (Zwillinger and Kokoska, 2000). For overall study area slopes, skewness ranged from approximately symmetric (L3, N, U2, L2, U1) to moderately left skewed (U3, U4, U5, L1) (Table 4, column 3). The upland terrains (U3, U4) had left-skewed distributions of slopes. Slopes of source zones

465 varied from approximately symmetric (U5) to moderately (L3, N) to highly right skewed (U1, U2, U3, U4, L1, L2) (Table 4, column 6). The distribution of slopes in areas of non-channelized runout was moderately left skewed to highly right skewed (Table 4, column 9) and channelized runout was approximately symmetric (L1, U2, L2) to moderately left skewed (U1, N, L3, U3, U4, U5) (Table 4, column 12). Our results indicate there was no clear pattern in slope characteristics of landslide-affected areas related to geologic terrane or geomorphic terrain.

Results also show median source-zone slopes were not correlated with median slopes of the study area (Fig. 10a);
470 instead, they were relatively consistent across all study areas. There was some correlation between slopes of non-channelized runout zones (P_{10} and P_{50}) and median slope of study area (Fig. 10b).
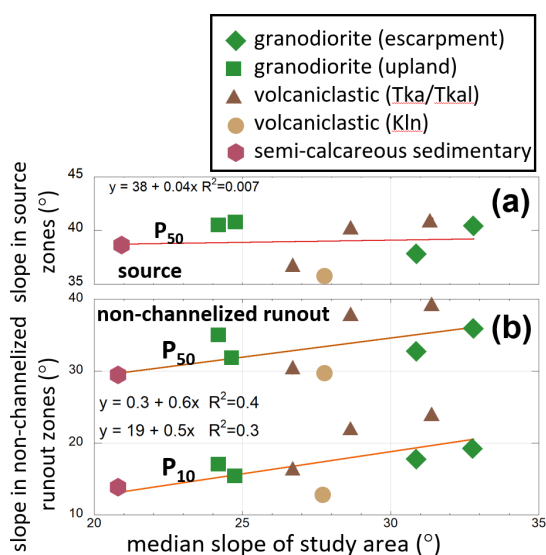

Figure 10. Median slope of study area related to slopes of a) landslide source zones and b) non-channelized runout zones.

5.4 Identification and characterization of channelized debris flows — Maria's most mobile (MMM)

475 We applied our two criteria to extract MMM from the published landslide inventories in the nine study areas. Figure 11 highlights landslides with > 40% of runout area located in close proximity (5 m) to a channel, including some non-channelized, lower mobility landslides (Fig. 10b). Figure 12 highlights MMM in the context of the two criteria.

Natural Hazards
and Earth System
Sciences
Discussions
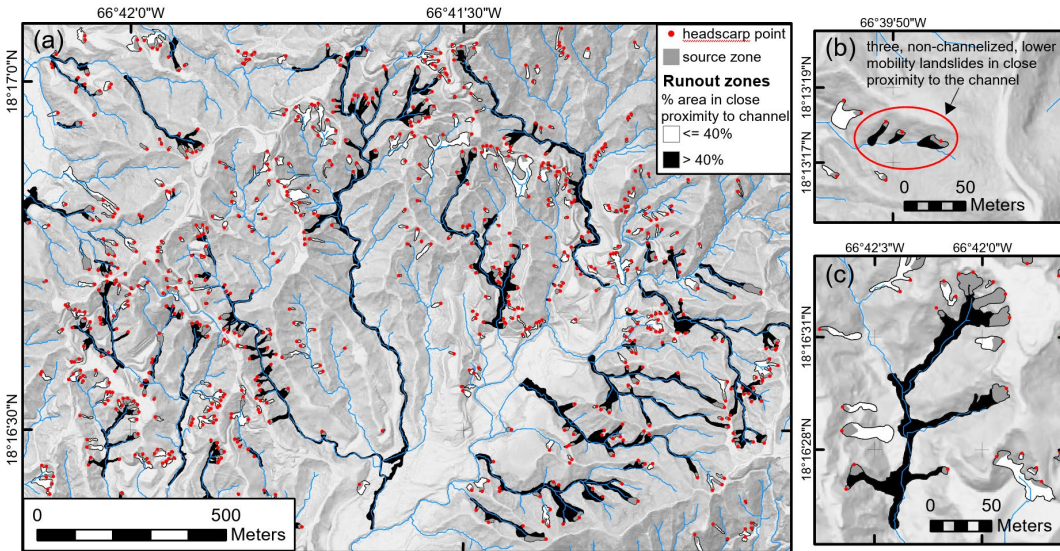
Figure 11. Portrayal of some of Maria's most mobile debris flows. a) Map view of study area U1 showing 761 mapped landslide headscarp points (red points), associated source zones (dark gray), and 391 runout zones (Bessette-Kirton et al., 2019b; Einbund et al., 2021b). Runout zones with > 40% runout area located in or in close proximity to the channel are shown in black and those with < 40% in white. b) Zoomed-in view of study area U4, showing lower mobility landslides with short runout length, identified as having > 40% runout length in the channel. c) Zoomed-in view illustrates multiple landslide sources coalescing to a single debris-flow runout zone.
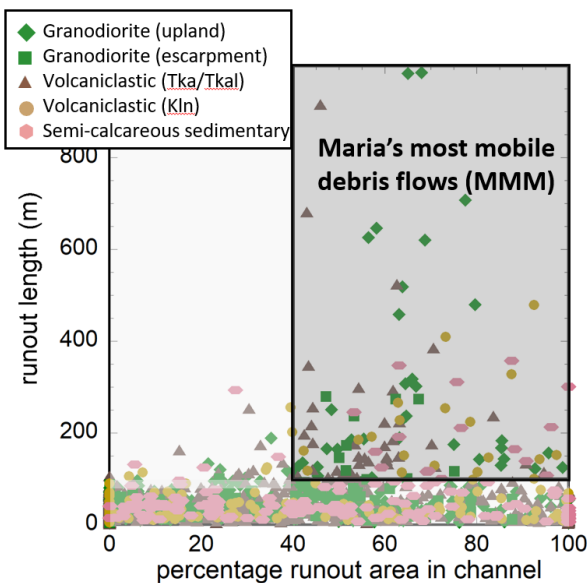
Figure 12. Runout length and percentage of runout area in designated channels, for channelized runout zones in all study areas, grouped by geologic terrane. Gray box highlights MMM, identified by the characteristics of > 40% runout area in close proximity to the channel and > 100 m runout length.

Table 6 summarizes the quantities and percentages of 1) landslide source areas (landslides) associated with MMM (columns 1,2, and 3) and 2) runout zones meeting the MMM criteria (columns 4, 5, and 6), where the influence of coalescence

21

Natural Hazards
and Earth System
Sciences

Discussions

Open Access

EGU

(Fig. 11c) results in multiple landslides contributing to a single runout path. Here, the runout zones may contain both non-channelized and channelized runout. We found that the percentage of landslide source areas associated with MMM ranged from 8.1% to 30% in different study areas. The study areas with three highest percentages, U1, N, and L2, are located in three different geologic terranes; here, 30%, 24.8% and 24.6% of landslides met the MMM criteria, respectively. The percentage of

495   runout zones meeting the criteria for MMM ranged from 3.3% to 9.0%, with the highest percentages found in three different geologic terranes, study areas U5, N, and U2; in this case the percentage of runout zones was 9.0%, 7.2%, and 6.7%, respectively. Study areas in other geologic terranes (L2, U1, U4, and L3) had slightly smaller percentage (5.2% to 5.6%) of runout zones identified as MMM; L1 and U3 had the smallest values, with 4.3% and 3.3% of runout zones identified as MMM. Our results highlight several observations for channelized debris flows triggered by Hurricane Maria: 1) channelized debris flows

500   are a minority of the landslides, 2) all geomorphic terrains and geologic terranes have some channelized debris flows, 3) escarpment terrains have a higher percentage of landslides associated with the MMM criteria, in comparison with upland terrains, 4) the percentage of runout zones does not show any consistent trends, and 5) there is no distinct pattern related to geologic terrane. Areas with a high landslide density, such as some of the escarpment terrains, may have many landslides in close proximity, thereby increasing the potential to coalesce in the nearest drainage. Given the influence of coalescence, the

505   percentage of landslides and percentage of runout zones (Table 6, column 3 and 6) did not correlate.

Table 6. Number and percentage of landslides and runout zones meeting the most mobile (MMM) criteria for nine study areas, sorted by percentage of landslides associated with MMM.

		# landslides (1)	# landslides associated with MMM (2)	% landslides associated with MMM (3)	# runout zones (4)	# runout zones with MMM criteria (5)	% runout zones with MMM criteria (6)
◆	U1	761	228	30.0%	391	21	5.4%
●	N	440	109	24.8%	263	19	7.2%
▲	L2	480	118	24.6%	306	17	5.6%
▲	L3	288	57	19.8%	210	11	5.2%
◆	U2	382	71	18.6%	238	16	6.7%
▲	L1	525	87	16.6%	375	16	4.3%
■	U3	191	29	15.2%	90	3	3.3%
⬡	U5	168	20	11.9%	156	14	9.0%
■	U4	124	10	8.1%	130	7	5.4%
	all	3235	719	22.2%	2159	124	5.7%

Our results from 124 debris-flow inundation zones (Table 7) show that MMM typically (P_{50}) occur in stream reaches

510   with stream order ≤ 2; all MMM occur in stream reaches with stream order ≤ 5 (Table 7). MMM have mean stream slopes of about 5 to 16°, mean planform curvature of 0.03 m^{-1}, and a mean P_{src} of 58% to 85%. Less common, but more extreme

Natural Hazards
and Earth System
Sciences

Open Access

EGU

Discussions

endmembers of MMM have a stream order of 4 or 5, stream slope of 0.2 to 7.0°, planform curvature from a smoothed DEM of

0.0 to 0.02 m^{-1}, and P_{src} of 9% to 33%. These results provide criteria to define debris-flow growth zones for inundation scenarios.

515

Table 7. Percentiles of maximum Strahler stream order, mean stream slope, mean planform curvature, and mean percentage contributing area susceptible to shallow landslides (P_{src}) for debris-flow inundation zones. Values are based on the mean or maximum (for stream order) value along runout path of MMM.

| parameter	percentile	Lares (L1, L2, L3)	Utuado (U1, U2, U3, U4)	Naranjito (N)	Utuado (U5)
maximum Strahler stream order	P_{50}	2	3	2	2
	P_{75}	3	3	3	3
	P_{90}	4	4	4	4
	P_{100}	5	5	4	4
mean stream slope (degrees)	P_{50}	15.9	9.8	15.0	4.6
	P_{25}	11.2	7.0	11.2	1.7
	P_{10}	8.2	4.8	8.8	0.9
	P_{0}	3.1	1.1	7.0	0.2
mean planform curvature (m^{-1})	P_{50}	0.03	0.03	0.03	0.03
	P_{25}	0.02	0.02	0.02	0.01
	P_{10}	0.02	0.01	0.01	0.01
	P_{0}	0.01	0.01	0.01	0.00
mean percentage contributing area susceptible to shallow landslides (P_{src})	P_{50}	85%	79%	58%	75%
	P_{75}	77%	65%	42%	52%
	P_{90}	62%	55%	20%	29%
	P_{100}	33%	29%	9%	14%

6 Results of runout and inundation modeling

6.1 H/L scenarios

520

For the mapped study areas, consisting predominantly of highly dissected topography, steep slopes, and narrow valleys, even large changes in α did not greatly modify zones of *H/L* runout. Figure 13 illustrates where there is some minimal additional runout area with a substantial decrease in α from 30 to 20°. Significant areas on the hillslope are encompassed by *H/L* runout zones in the range of 25 to 30° (Fig. 13, brown zones) derived from Hurricane Maria source areas, whereas, when α is < 20°, the affected areas (Fig. 13, blue zones) are located within narrow channel bottoms. A decrease to 20° captures additional area within the non-channelized runout zones of mapped landslides, without a significant increase in areas identified as susceptible (added yellow areas). The area shown in figure 13 is representative of the majority of areas where landslide inventories were available. Appropriate choice of α for regional maps is controlled by the slope angle of topography upslope of channels, quantified in our analysis of slopes in mapped non-channelized runout zones (Table 4, columns 7 and 8). Our analysis of slopes in these zones indicates a wide range of potential α values. To eliminate the potential for gaps between estimated non-channelized runout areas and channelized debris-flow inundation areas, we selected α = 20° for our susceptibility maps.

525

530
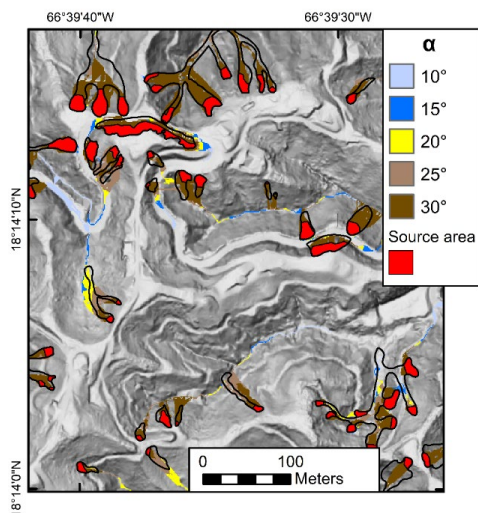
Figure 13. *H/L* runout results for a range of α values (10, 15, 20, 25, and 30°) in a section of U2, an escarpment study area in the granitoid terrane, Utuado. Source areas from Einbund et al., 2021b.

535

6.2 Debris-flow inundation scenarios

Our evaluation of eight debris-flow inundation scenarios (Fig. 6) indicates that modification of the parameters defining debris-flow growth zones can have a significant influence on the pattern and extent of inundation. For example, purple zones in Fig. 14a illustrate the inundation area where debris-flow growth zones extended lower in the drainage network, as controlled by a larger value for maximum stream order and smaller value for minimum stream slope. Maximum volume (V_{max} = 1000 m^3) and growth factor (c_1 = 0.01 m^3 m^{-2}) are held constant in scenarios A-1k, B-1k, C-1k, and E-1k. In the case of relatively wide basins and multiple incoming tributaries, more generous growth zones

540

create greater runout lengths (Fig. 14a). In the same topography, increased growth factors with a fixed growth zone also create longer and wider inundation zones (Fig. 14b).

545   In contrast, narrower drainage basins with few contributing tributaries that abruptly exit steep mountainous terrain into a wide, flat valley over a short distance, exhibited no difference between results with highly variable definition of growth zones. Fig. 14c demonstrates this situation, where scenario B-1k, C-1k, and E-1k produce identical inundation results. Scenarios C-1k, C-3k, and C-10k, with increasing growth factor (c_1 of 0.01, 0.05 and 0.2 m^3 m^{-2}, respectively) and V_{max} (1000, 3000, and 10,000 m^3, respectively) produce progressively wider and longer runout length regardless of basin shape (Figs. 14c, d), where increased c_1 produces wider inundation zones higher in the drainage network. Increased V_{max} can produce both wider and longer inundation zones. In these scenarios, debris-flow growth will always be halted

550   when the maximum stream order or minimum stream slope criteria for a given scenario is achieved, yielding a volume proportional to the upslope area susceptible to landsliding. Therefore, growth zones that terminate before V_{max} is achieved will have smaller areas of inundation.
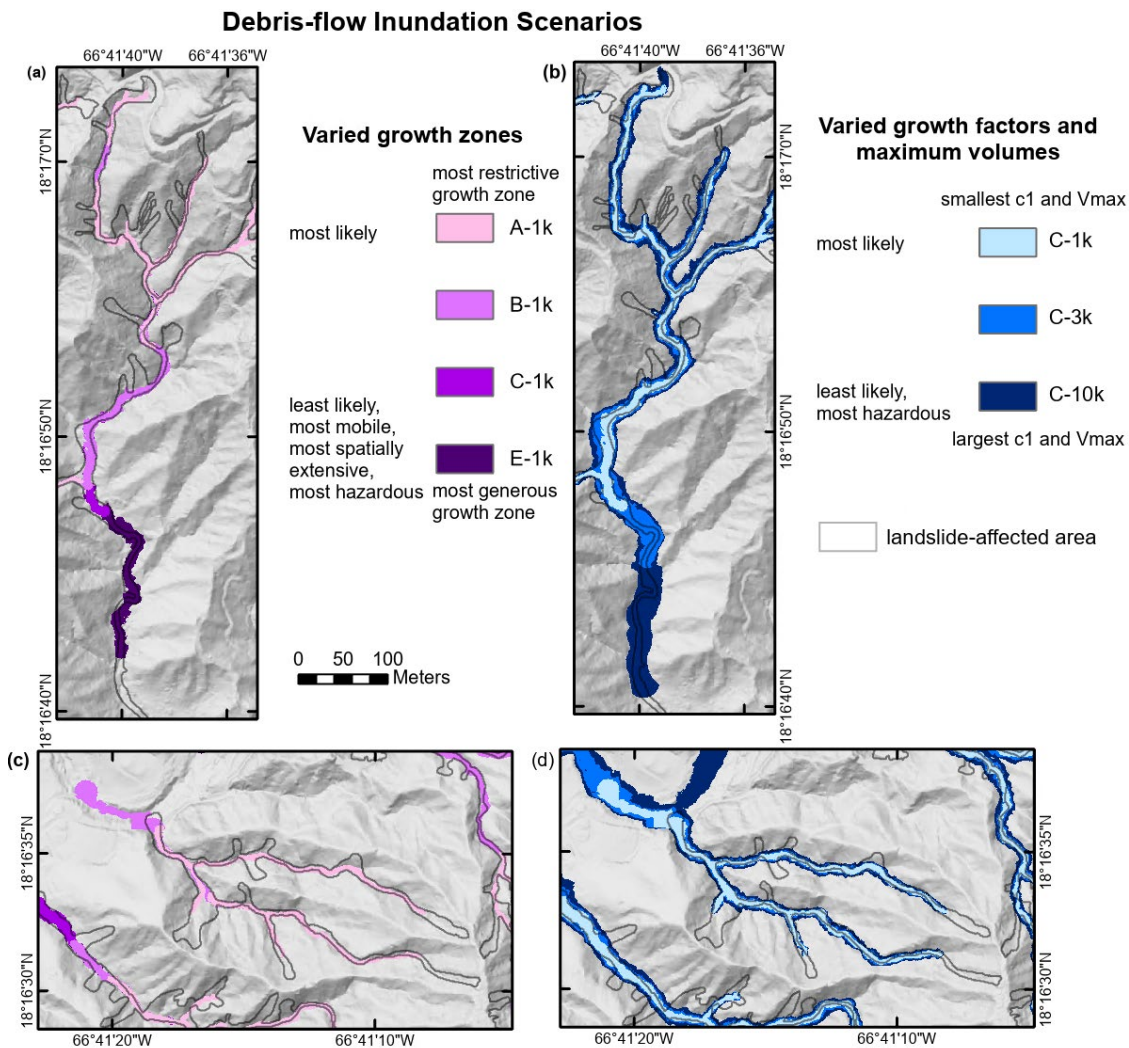
**Figure 14. Results from debris-flow inundation scenarios with varied growth controls in different topographies. a) Wider topography**
555   **with varied growth zones. A-1k, B-1k, C-1k, and E-1k showing progressively greater inundation lengths with more generous growth zones. b) Wider topography with increasing growth factors and maximum volumes. C-1k, C-3k, and C-10k showing progressively**

wider and longer inundation lengths with increased growth factor and maximum volume (V_{max}). c) Narrower basin with fewer

incoming tributaries and varied growth zones. Here, B-1k, C-1k, and E-1k produce identical results, only A-1k differs. d) Narrower

basin with increasing growth factors. Regardless of basin shape, C-1k, C-3k, and C-10k produce progressively wider and longer

560   inundation lengths. Black outlines are mapped landslides from Hurricane Maria including source areas (Einbund et al., 2021b). The

scale bar is the same for all panels.

6.3 Evaluation of predictive success for debris-flow inundation scenarios

Figure 15 shows our ROC analysis for the eight scenarios, evaluated for all MMM. Solid gray lines show positive likelihood

ratio ($PLR = TPR/FPR$), where higher PLR indicates a higher likelihood of correct prediction. Dashed gray lines show distance

565   from the upper left corner, the location of perfect classification. False positive rate (FPR) may be over-estimated in cases where

the actual terminus of debris-flow deposits could not be identified.
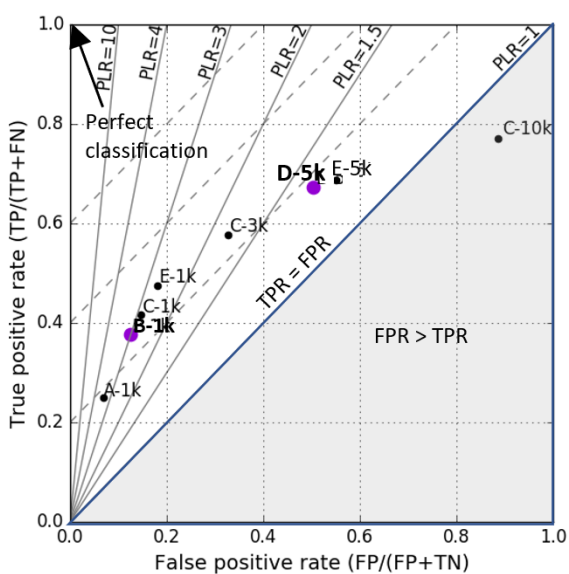
Figure 15. Receiver Operator Characteristic (ROC) plot for eight debris-flow inundation scenarios evaluated for nine study areas

affected by MMM. The two scenarios selected for regional susceptibility maps are highlighted in purple. Scenario B-1k is a likely

570   **scenario and D-5k is a less likely, but more hazardous scenario.**

For our regional susceptibility maps, we first selected a scenario (B-1k) with relatively high value for PLR (Fig. 15,

PLR = ~3). This scenario, B-1k, defines zones of extremely high susceptibility to debris-flow inundation. Scenario B-1k

minimizes over-prediction, as characterized by relatively low FPR and high PLR. TPR based on the area affected is ~0.38,

whereas consideration of the number of debris-flow inundation runout zones provides more impressive TPR values, ranging

575   between 0.50 and 0.95 (Table 8). TPR was lowest for U5, the largest study area with a very low percentage of area affected by

landslides (Table 3). Overall, for all study areas combined, scenario B-1k, identified 85% of debris-flow inundation zones.

To aid selection of a more extensive scenario, we examined scenarios in map view, in combination with a ROC plot

(Fig. 15). We selected D-5k because it provides an increased true positive rate (TPR) before the significant decrease in positive

likelihood ratio (PLR) seen with scenario E-5k. Scenario D-5k identified 90% (TPR = 0.90) of debris-flow runout zones (Table

580   8). This TPR of 0.90 is in alignment with the TPR selected for source-area susceptibility thresholds (Baum et al., 2024). Scenario

D-5k defines a more hazardous, but less likely, scenario representative of the area affected in the most severely impacted

drainages during Hurricane Maria.

Table 8. Number of debris-flow inundation zones (MMM) and *TPR* for the two selected susceptibility scenarios. MMM are grouped by geologic terrane.

	# debris-flow inundation zones (MMM)	*TPR* for number of detected debris-flow inundation zones	
		B-1k	D-5k
Lares (L1, L2, L3)	44	0.95	0.95
Utuado (U1, U2, U3, U4)	47	0.83	0.89
Utuado (U5)	14	0.50	0.71
Naranjito (N)	19	0.89	0.89
All study areas combined	124	0.85	0.90

585

6.4 Susceptibility maps portraying three mobility zones

We applied our linked-model approach to create regional susceptibility maps delineating potential locations of landslide initiation, downslope runout, and debris-flow inundation during prolonged, intense rainfall, for Lares, Naranjito, and Utuado municipalities, encompassing a total area of 560 km^2. Potential source areas (initiation) from shallow landslide susceptibility

590 modeling (Baum et al., 2024) were used to identify 20° *H/L* runout zones and upslope contributing source areas for volume estimations (Eq. (4)) used in debris-flow inundation scenarios B-1k and D-5k.

In our regional susceptibility maps (e.g., Fig. 16), debris-flow inundation areas (purple zones) overlie all other zones and may conceal underlying source (red) and *H/L* runout zones (yellow); non-channelized runout zones (*H/L*) underlie all other colors in the perspective view. Debris-flow inundation zones are shown in two shades of purple, where dark purple is scenario B-

595 1k, highlighting inundation in upper parts of the drainage network, and light purple is scenario D-5k. In steep, dissected escarpment terrains, such as U1, most of the topography meets the criteria for source zones, resulting in substantial overlap between areas susceptible to shallow landslides and *H/L* runout zones.

Natural Hazards
and Earth System
Sciences
Discussions
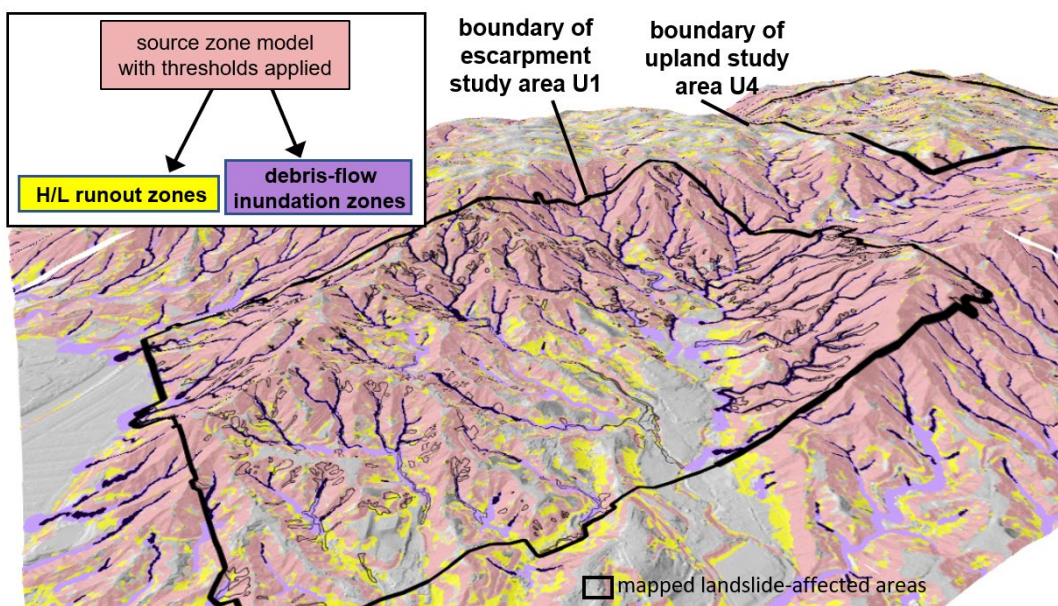
Figure 16. Perspective view of landslide susceptibility results in part of Utuado encompassing study area U1 (2.5 km², located on an escarpment, and study area U4, located in an upland terrain. Mapped landslides (Bessette-Kirton et al., 2019b; Einbund et al., 2021b) shown for reference with black outlines. Dark purple is scenario B-1k and light purple is the more extensive scenario D-5k. Approximate location at center of image is 18° 16′ 40″ N, 66° 41′ 10″ W.

In open-slope topographies, the absence of channelization controls the applied modeling approach and resulting susceptibility. Figure 17 shows a comparison of landslide-affected areas (Fig. 17a) and modeling results (Fig. 17b). Here, susceptibility results show H/L runout for non-channelized areas; debris-flow inundation is not modeled.
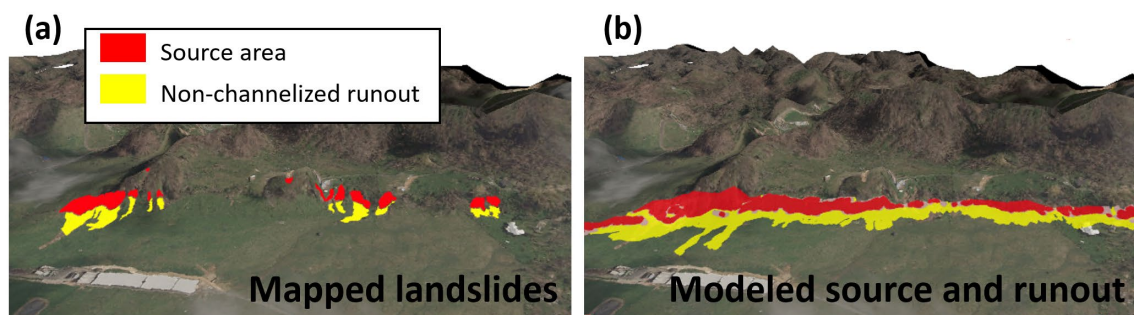
Figure 17. Perspective view of post-Maria aerial imagery draped on DEM in a non-channelized open-slope topography in Northern Utuado. a) Mapped landslides located in semi-calcareous sedimentary units adjacent to karst topography in northern Utuado (Baxstrom et al., 2021a) divided into source and non-channelized runout, b) Runout modeling results of areas susceptible to shallow landslides (Baum et al., 2024) and H/L runout zones (yellow). Approximate location at center of image is 18° 18′ 5″ N, 66° 49′ 0″ W.
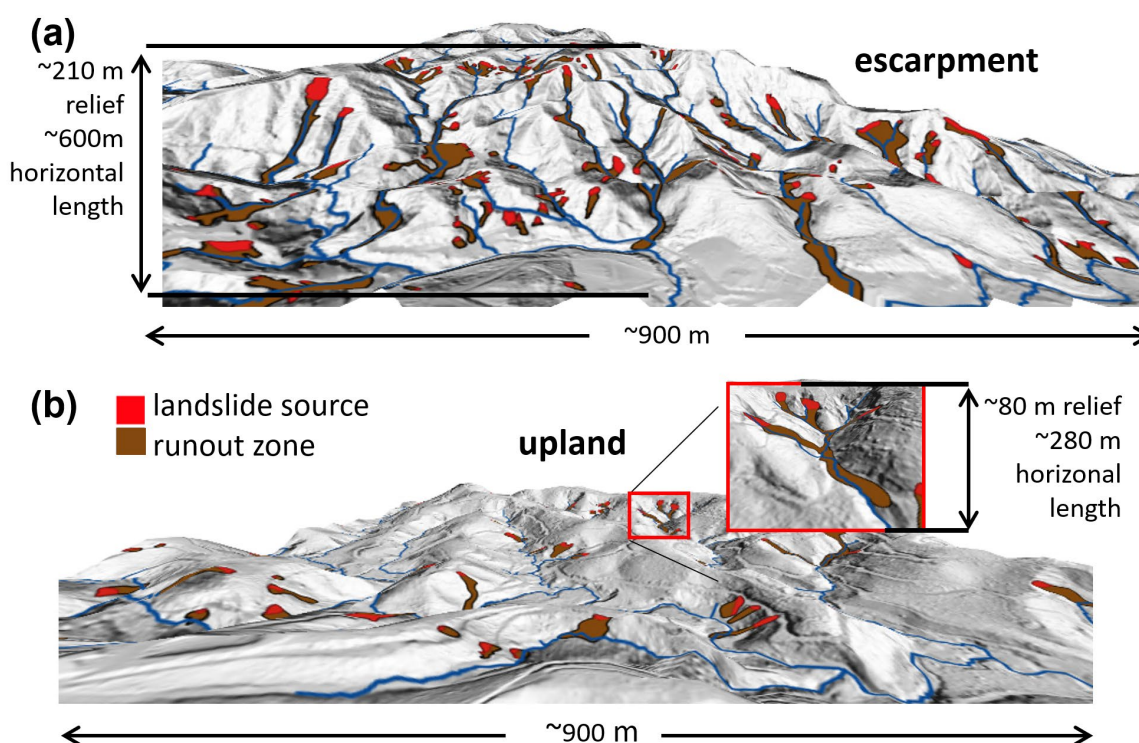
7 Discussion

We used three zones of landslide mobility as the framework for topographic analysis and a linked-model approach to estimate areas susceptible to landslide runout. Both non-channelized and channelized landslide runout were observed in Hurricane Maria (Figs. 1, 4, 7) and have the potential to adversely impact roads and infrastructure.

7.1 Insights from topographic analysis

Our topographic analysis of landslide-affected areas quantified the area affected within each mobility zone and provided statistics describing the topographic slopes in each zone. Study areas with the highest percentage of area susceptible to landslides had the largest area affected by landslides during Maria (Table 3, Fig. 8). The percentage of total landslide-affected area to percentage of study area with steep slopes (Fig. 8b,c) increases at a greater rate (from 0.3% to 8%; Table 3, column 7) than the more modest increase (from 0.1% to 2%; Table 3, column 4) of the percentage of study area affected by landslide source areas only. This disproportionate increase in total affected area with a high percentage of steep slopes suggests increased mobility and greater hazard in these areas, in contrast to more isolated steep slopes. The statistical distribution of topographic slopes shows that the escarpment study areas (U1 and U2) did not have steeper source areas than upland terrains (Table 4, column 4 and 5), although the overall slopes are steeper in the escarpment areas. These combined observations indicate differences are not due solely to slope angle, material strengths, hydrologic properties or conditions, but also to predisposing factors related to geomorphic setting. Possible explanations for this phenomenon might include coalescence (e.g., Coe et al., 2021), more readily available entrainable material due to frequent landslides (e.g., Coe et al., 2021; Scheip and Wegmann, 2022), soil depths, and/or topographic controls (e.g., Corominas, 1996; Coe et al., 2011). Escarpment terrains, with more terrain susceptible to landslides,

630   provide more opportunity for the coalescence of contributing landslide source areas over a greater length of runout path, either channelized or non-channelized. Debris-flow runout paths may traverse a substantial distance through areas of additional contributing landslide source area. In addition, individual basins in escarpment terrains (Fig. 18a) have higher topographic relief than dissected uplands (Fig. 18b). Higher relief provides the potential for greater runout lengths before there is a change in stream slope conducive to deposition — this results in correspondingly larger runout areas (Fig. 8). Likewise, areas with high

635   drainage density will provide greater opportunity to amalgamate multiple flows, potentially having a nonlinear impact on access to readily entrainable material.

(a)
~210 m relief
~600m horizontal length
escarpment
~900 m

(b)
■ landslide source
■ runout zone
upland
~80 m relief
~280 m horizonal length
~900 m

Figure 18. Perspective views showing mapped landslide source and runout zones caused by Hurricane Maria in Utuado, Puerto Rico
640   **(data from Einbund et al., 2021b): a) escarpment terrain in study area U1, and b) upland terrain in study area U3. Approximate location of a at center of image is 18° 16′ 30″ N, 66° 41′ 20″ W; b is located at 18° 16′ 30″ N, 66° 47′ 35″ W.**

7.2 Mobility metrics

Mobility metrics can be used to quantify relative landslide mobility or predict the potential for future mobility. At initiation, the
645   potential for landslide mobility is controlled by material properties, pore pressures, and initial porosity of the material (e.g., Iverson, 1997; Iverson et al., 2000; Reid et al., 2008; Iverson et al., 2011; Collins and Reid, 2020). Mobility can be further enhanced by relatively high initial moisture content of the material over which a debris flow travels (Iverson et al., 2011; Reid et al., 2011), proximity to a channel network (e.g., Coe et al., 2011), and channel confinement (e.g., Iverson, 1997). In addition, topographic constraints such as height of fall, regularity of the pathway, bends, deflections, and confinement can limit or enhance
650   landslide travel distance (e.g., Corominas, 1996).

Natural Hazards
and Earth System
Sciences
Discussions

EGU

Several mobility metrics have been discussed in the literature, including: unitless runout number ($L/A^{1/2}$) (Wallace et al., 2022), L, excessive travel distance (L_e) (Hsu, 1975; Corominas, 1996), relative excessive travel distance (L_r) (Corominas, 1996), H/L, angle of reach (α), L/H, and $V/A^{2/3}$ (e.g., Scheidegger, 1973; Hsu, 1975; Nicoletti and Sorriso-Valvo, 1991; Corominas, 1996; Iverson et al., 2015; Legros, 2002; Wallace et al., 2022). In Puerto Rico, the percentage of landslide-affected area (Table 3,

655   column 7 and Fig. 8) serves as a metric to compare overall landslide mobility between study areas.

The two debris flows shown in Fig.18 illustrate one potential problem with the use of H/L for assessing mobility. For the escarpment flow (Fig. 18a), $L = \sim600$ m and α = 19°, whereas for an upland terrain debris flow (Fig. 18b), $L = 280$ m and α = 16°. Lower α suggests greater relative mobility for dissected upland flow, despite its significantly shorter runout length. Thus, it can be difficult to determine if there is a fundamental difference in the initial potential for mobility (as measured by any metric)

660   or the ultimate mobility; rather, each debris flow traveled until a decrease in stream slope, sufficient for deposition, was reached. In these Hurricane Maria examples, topographic relief defines the H and L of travel before a decrease in stream slope thereby controlling the ultimate mobility of these flows.

In our linked-model approach, topographic factors are automatically incorporated via multiple mechanisms. H/L runout zones are inherently controlled by local topography and in channelized topography, minimal additional runout area is modeled

665   with decreased α (as illustrated in Fig. 13). In channelized topography, debris-flow growth is restricted to drainages with sufficient stream slope and greater than 20% of upslope contributing area susceptible to shallow landslides (P_{src}). These restrictions, thereby provide a self-regulating method to estimate potential inundation. Likewise, most channelized debris flows will continue along their pathway until reaching a significant decrease in channel slope, after which deposition is predominant. This concept is applied in our inundation modeling, without the need to define spatially variable input parameters.

670   **7.3 Considerations for linked-model approach**

7.3.1 Selection of angle of reach

Although much debate exists in the literature regarding the application of the angle of reach (α) (e.g., Hungr et al., 2005), H/L is commonly used to quantify relative mobility of landslides. As noted by Wallace and Santi (2021), there are potential limitations to the usefulness of H/L to describe landslide mobility. Specifically, unless there is a change in gradient downslope of the source,

675   H/L only measures the overall slope gradient and does not distinguish between short- and long-runout events on uniform slopes. We found a correlation between slopes of non-channelized runout zones (P_{10} and P_{50}) and median (P_{50}) slope of study area (Fig. 10b), an indication that local topography can influence H/L runout angles, an important factor to consider when evaluating statistics of runout angles from landslide inventories. Herein, we do not use H/L or L to compare mobility between landslides as these metrics are also highly dependent on basin shape, relief of basin, angle of intersection with tributary junctions, and type of

680   landslide (e.g., Corominas, 1996). However, the subtleties of H/L measurements complicate the selection of α for our modeling application. To address these complications, we assessed a wide range of H/L values at 5° increments of α (Fig. 13) and considered the amount and locations of additional runout area. In many of the study areas with steep, dissected topography, we observed that most non-channelized runout is encompassed by H/L runout zones identified with α > 25°. Some additional non-channelized runout is within the zone between 20° and 25°. Additional areas encompassed by a value less than 20° typically are

685   located in the channel, where our methods for debris-flow inundation were applied. In open-slope topographies, where very few mapped landslide-affected areas were available for quantitative assessment, our choice of α = 20° compares well visually with observed runout from Hurricane Maria (Fig. 17).

In addition, world-wide datasets of H/L (e.g., Corominas, 1996) provide useful relative comparison of some the most notable documented landslides in the literature. Many types of landslides, including rockfalls, translational slides, debris flows,

690   earthflows, mudslides, and rock avalanches, display a reduction in α with increasing volume (e.g., Corominas, 1996; Iverson et
        al., 2015). The further application of reduced α with increasing volume can be employed with our methods to refine estimates of
        areas susceptible to non-channelized runout.

7.3.2 Selection of debris-flow growth zones

        Selection of debris-flow growth zones controls where debris-flow growth factors are applied. The location of these zones can
695   impact inundation patterns and extent as significantly as the choice of c_1 or V_{max} (Fig. 14). In some cases, stream slope can serve
        as a single control on location of these growth zones. Reid et al. (2016) summarized slopes where deposition was predominant
        from previous studies, with deposition for confined flows occurring at slopes less than 15°, and in some cases as low as 1°. More
        recent studies provide stream-slope thresholds in a similar range. For debris flows in North Carolina, Scheip and Wegman (2022)
        found a transition from erosion to deposition in the range of 8° to 30°, with a mean value of 18°. Burns et al. (2022) identified
700   that debris-flow transport (non-deposition) occurs either on steep (> 8°) channel reaches or highly confined reaches with gentler
        slopes (< 5°). In Puerto Rico, field measurements of locations where growth transitioned to deposition (3° to 8°) guided our
        selection of stream slopes for growth zones (Coe et al., 2021).

                In the diverse topography of Puerto Rico, complexities such as short segments of steep stream slopes distanced from
        areas of landslide susceptibility, and locally isolated areas susceptible to landslides, necessitated multiple parameters to restrict
705   growth zones. We used characteristics of MMM inundation zones to constrain growth zones for our debris-flow inundation
        modeling. Statistics based on analysis of MMM provided ranges of values for Strahler stream order, percentage of contributing
        area susceptible to debris flow (P_{src}, Eq. (1)), and planform curvature (Table 7). Stream reaches with high values of P_{src}, are
        directly coincident with locations where the most susceptible areas are located, and this parameter might be used as the primary
        control to define growth zones.

6.3.3 Selection of debris-flow growth factors and volumes

        Volume estimates within zones of debris-flow growth are controlled by debris-flow growth factors and limited by V_{max} .
        Published values for growth factors (sometimes termed "growth rates") are typically estimated from differences in elevation
        calculated from photogrammetry or lidar-derived DEMs (Reid et al., 2016; Coe et al., 2021; Scheip and Wegman, 2022). Reid et
        al. (2016) summarizes published length-based growth factors and applies length- and area-based growth factors for Oregon, with
715   values ranging from 11–24 m^3 m^{-1} and 0.12–0.2 m^3 m^{-2}, respectively.

                For Hurricane Maria, estimates of c_1 and V_{max} based on difference of DEMs from pre- and post-Maria lidar were
        available (Coe et al., 2021). Our calculation of growth factors normalized to contributing susceptible area rather than full
        contributing area (Table 2) allows the application over large areas, where susceptibility to shallow landslides is spatially variable.

                For our assessment of debris-flow inundation scenarios, we found that the scenario with the largest maximum volume
720   estimate (C-10k), resulted in a false positive rate that exceeded the true positive rate, indicating severe overprediction (Fig. 15).
        The maximum volume for C-10k originated from a site with significant volume contribution from a single landslide and minimal
        contribution from debris-flow growth mechanisms (Four Car site, Coe et al., 2021). In this situation, our area-integrated growth
        factor will under-estimate volume at the site of channel initiation and over-estimate growth along the travel path. In regions
        where these characteristics are known to be the predominant pattern, smaller growth factors, power-law growth factors, or initial
725   source volumes can be applied to our methodology.

                Future investigations of debris-flow growth factors could help determine the applicability of growth-factors beyond the
        specific basins for which they were calculated. Likewise, questions related to whether the same basins will repeatedly generate

debris-flows of the same magnitude or may have a delay in time after a storm event has removed readily entrainable material

from the channels is an important consideration. In addition, the susceptibility of different drainage basins with seemingly

730   similar characteristics may depend on human modifications within each basin.

7.3.4 Assessment of debris-flow inundation scenarios

Contingency table metrics provide multiple evaluation criteria (e.g., Powers, 2011). Choosing a metric for optimization of

scenarios depends on the objectives — selection of a high value for *TPR* maximizes the number of true positives (*TP*) and

provides high success in prediction of susceptible areas. Unfortunately, selection of a scenario based solely on *TPR* typically

735   contributes to a higher value for *FPR* (Fig. 15) and can result in assignment of significant area not affected by actual landslides

in a given landslide-inducing event as susceptible. In the case of landslide modeling, although this may be a false prediction for a

specific previous event, the results may produce successful prediction in a future event. Typically, only a small percentage of

area susceptible to landslide initiation or runout is affected by a single event. For example, in Hurricane Maria, only 0.4% to

3.3% of steep slopes were subject to landslides (Table 3).

740   When available, information regarding the specific locations of landslide initiation and stream reaches where readily

entrainable material is available can be incorporated into our methods. For example, Jibson (1989) noted channel scouring and

side-slope debris contributed 90–95% of debris-flow volume in debris flows along the south-central coast of Puerto Rico, during

a tropical storm on October 5–8, 1985. Although generalized parameters provide a good initial estimate, field observations and

debris flow history can focus on locations where conditions conducive to enhanced debris-flow growth are present. Field

745   observations have the potential to highlight basins with elevated level of hazard and improve predictive success of modeling

results.

7.4 Limitations of linked-model approach

Our methods are not a replacement for site-specific investigations or cases where physics-based models can be calibrated to

provide more detailed information, including estimates of velocity and inundation depth (e.g., McDougall and Hungr, 2004;

750   Christen et al., 2010; George and Iverson, 2014; Iverson and George, 2014; FLO-2D Software Inc., 2017; Barnhart et al., 2021).

Our methodology is designed to assess large regions for runout and debris-flow inundation hazard. In areas of high concern, field

studies, analysis of past events, and application of physics-based models may provide more refined hazard estimates.

The advantages of our modeling approach include the ability to estimate areas susceptible to runout and inundation

without the need to invoke spatially variable angles of reach, debris-flow growth zones, or debris-flow growth factors based on

755   material properties. Our linked-model approach successfully estimated runout susceptibility for three municipalities in Puerto

Rico, where knowledge of site-specific materials and conditions was limited.

8 Conclusions

Our analysis of landslide-affected areas from Hurricane Maria illustrates that both non-channelized and channelized landslide

runout (debris-flow inundation) occurred across nine study areas, encompassing escarpment and upland terrains in volcaniclastic,

760   granitoid, and non-limey sedimentary geologic terranes. Non-channelized runout was the most recurrent, whereas channelized

runout was the most areally extensive. Using the concept of zones of mobility, we analyzed topographic characteristics of

landslide-affected areas and applied an empirical, linked-model approach to estimate areas susceptible to non-channelized and

channelized runout. Our linked-model approach provided a self-regulating method, whereby topography controls the runout method, spatial distribution, and extent of potential landslide runout and debris-flow inundation zones in four primary ways:

765   1. The presence or absence of a channel network controls the application of runout method, where areas susceptible to non-channelized runout are identified by a minimum angle of reach and channelized debris-flow inundation zones are estimated using debris-flow growth factors combined with volume-area relations.

2. *H/L* runout zones provided a transition from source zones to channels and identified non-channelized runout in areas with open-slope topography, where channels are not present.

770   3. In channelized topography, debris-flow growth zones were restricted to steep stream reaches (> 5°) possessing characteristics of Hurricane Maria's most mobile debris flows (MMM): low stream order (≤ 4), high percentage of contributing area susceptible to debris flows (> 20% P_{src}), and concave planform curvature (< 0.02 m^{-1}).

4. Within the zones of debris-flow growth, volumes were calculated as a function of upslope area susceptible to shallow landslides, whereby drainage basins with minimal susceptible area are assigned smaller volumes and highly susceptible

775   areas are assigned larger volumes, up to a specified maximum, V_{max}. The rate of debris-flow growth is controlled by a growth factor, c_1.

Our coupled-model approach incorporates these methods for portraying runout and inundation for landslides over a range of mobility and enables runout assessment over large regions without the computational effort required by physics-based models or the need to identify precise locations and volumes of landslide sources. To provide an assessment of areas susceptible to

780   landslide runout and inundation, we applied our two runout models in three municipalities that had high landslide density from Hurricane Maria: Utuado, Lares, and Naranjito, covering a total area of 560 km^2.

Our results illustrate that that geomorphic setting can exert a primary influence on debris-flow runout. Escarpment terrains, with high relief and a high percentage of contributing area susceptible to shallow landslides, were predicted to have larger areas affected by long-runout debris flows in contrast to dissected-upland terrains. These patterns match observations from Hurricane

785   Maria. Assessment of the predictive success of our debris-flow inundation modeling, based on 124 debris flow runout zones from Hurricane Maria's most mobile debris flows in all terrains, demonstrates that one of our scenarios identified 90% of the Hurricane Maria debris-flow runout zones.

Code availability

Computer codes used for this study are available in a U.S. geological Survey software repository (Cronkite-Ratcliff et al., 2024).

790   **Data availability**

Pre- and post- Hurricane Maria lidar-derived DEMs are available through the national map at https://apps.nationalmap.gov/lidar-explorer/ (U.S. Geological Survey 2018, 2020a,b,c). Landslide inventories are available as U.S. Geological Survey Data Releases (Bessette-Kirton et al., 2019b; Baxstrom et al., 2021a, 2021b; Einbund et al., 2021a, 2021b). Hurricane Maria's Most Mobile (MMM) landslides are also available as a U.S. Geological Survey Data Release (Brien et al., 2024).

Natural Hazards
and Earth System
Sciences

Discussions

References

Barnhart, K.R., Jones, R.P., George, D.L., McArdell, B.W., Rengers, F.K., Staley, D.M., and Kean, J.W.: Multi-model comparison of computed debris flow runout for the 9 January 2018 Montecito, California post-wildfire event, Journal of Geophysical Research, Earth Surface, 126(12), https://doi.org/10.1029/2021JF006245, 2021.

Baum, R.L., Savage, W.Z., and Godt, J.W.: TRIGRS—A Fortran program for transient rainfall infiltration and grid-based regional slope-stability analysis, version 2.0, U.S. Geological Survey Open-File Report, 2008-1159, 75 p., https://doi.org/10.3133/ofr20081159, 2008.

Baum, R.L., Cerovski-Darriau, C., Schulz, W.H., Bessette-Kirton, E.K., Coe, J.A., Smith, J.B., and Smoczyk, G.M.: Variability of Hurricane Maria debris-flow source areas in Puerto Rico—Implications for hazard assessment, American Geophysical Union Fall Meeting abstract #NH14A-02, 2018.

Baum, R.L., Brien, D.L., Reid, M.E., Schulz, W.H., and Tello, M.J.: Assessing Locations Susceptible to Landslide Initiation During Prolonged Intense Rainfall in the Lares, Utuado, and Naranjito Municipios of Puerto Rico, Nat. Hazards Earth Syst. Sci., 24, 1579–1605, https://doi.org/10.5194/nhess-24-1579-2024, 2024.

Bawiec, W.J., (Ed.): Geology, geochemistry, geophysics, mineral occurrences and mineral resource assessment for the Commonwealth of Puerto Rico, U.S. Geological Survey Open-File Report 98-38, https://doi.org/10.3133/ofr9838, 1998.

Baxstrom, K.W., Einbund, M.M, and Schulz, W.H.: Map data from landslides triggered by Hurricane Maria in a section of Naranjito, Puerto Rico, U.S. Geological Survey data release, https://doi.org/10.5066/P9GBGA4I, 2021a.

Baxstrom, K.W., Einbund, M.M., and Schulz, W.H.: Map data from landslides triggered by Hurricane Maria in the greater karst region of northwest Puerto Rico, U.S. Geological Survey data release, https://doi.org/10.5066/P9YYU7W1, 2021b.

Natural Hazards
and Earth System
Sciences
Discussions

Benda, L., Miller, D., Andras, K., Bigelow, P., Reeves, G., and Michael, D.: NetMap: a new tool in support of watershed science
and resource management, Forest Science, 53(2), 206-219, https://doi.org/10.1093/forestscience/53.2.206 , 2007.

830 Berti, M., Simoni, A.: DFLOWZ: A free program to evaluate the area potentially inundated by a debris flow, Computers &
Geosciences 67, 14-23, https://doi.org/10.1016/j.cageo.2014.02.002, 2014.

Bessette-Kirton, E.K., Cerovski-Darriau, C., Schulz, W.H., Coe, J.A., Kean, J.W., Godt, J.W., Thomas, M.A., and Hughes, K.S.:
Landslides triggered by Hurricane Maria: Assessment of an extreme event in Puerto Rico, GSA Today, 29(6), 4-10,
https://doi.org/10.1130/GSATG383A.1, 2019a.

835 Bessette-Kirton, E.K., Coe, J.A., Kelly, M.A., Cerovski-Darriau, C., and Schulz, W.H.: Map data from landslides triggered by
Hurricane Maria in four study areas of Puerto Rico, U.S. Geological Survey data release,
https://doi.org/10.5066/P9OW4SLX, 2019b.

Bessette-Kirton, E.K., Coe, J.A., Schulz, W.H., Cerovski-Darriau, C., and Einbund, M.M.: Mobility characteristics of debris
slides and flows triggered by Hurricane Maria in Puerto Rico, Landslides, 17, 2795–2809,
840 https://doi.org/10.1007/s10346-020-01445-z, 2020.

Bregoli, F., Ciervo, F., Medina Iglesias, V.C.D., Bateman Pinzón, A., Hurlimann Ziegler, M., Chevalier, G., and Papa, M.:
Development of preliminary assessment tools to evaluate debris flow risks, In XVIII International Conference on
Computational Methods in Water Resources, pp. 1-9, Centro Internacional de Métodos Numéricos en Ingeniería
(CIMNE), 2010.

845 Brien, D.L., Reid, M.E., Einbund, M.M., and Baxstrom, K.S.: Hurricane Maria's Most Mobile (MMM) landslides in nine study
areas in the Lares, Naranjito and Utuado Municipalities, Puerto Rico, U.S. Geological Survey data release,
https://doi.org/10.5066/P9NJ8MSP, in press 2024.

Brown, S.: Measures of Shape: Skewness and Kurtosis, https://Brownmath.com/Stat/Shape.htm , last access: 23 March 2022

Burns, W.J., Franczyk, J.J., and Calhoun, N.C.: Protocol for Channelized Debris Flow Susceptibility Mapping: Oregon
850 Department of Geology and Mineral Industries, Special Paper 53, https://www.oregongeology.org/pubs/sp/SP-53/p-SP-
53.htm, 2022.

Christen, M., Kowalski, J., and Bartelt, P.: RAMMS: Numerical simulation of dense snow avalanches in three-dimensional
terrain, Cold Regions Science and Technology, 63(1), 1–14, https://doi.org/10.1016/j.coldregions.2010.04.005, 2010.

Coe, J.A., Bessette-Kirton, E.K., Brien, D.L., and Reid, M.E.: Debris-flow growth in Puerto Rico during Hurricane Maria:
855 Preliminary results from analyses of pre- and post-event lidar data, in Cabrera MA, Prada-Sarmiento LF, Montero J,
(Eds.), Proceedings of the 13th International Symposium on Landslides, Cartagena, Colombia, International Society for
Soil Mechanics and Geotechnical Engineering, 8 p., https://www.issmge.org/uploads/publications/105/106/ISL2020-
7.pdf., last access: 9 March 2022, 2021.

Coe, J.A., Reid, M.E., Brien, D.L., and Michael, J.A.: Assessment of topographic and drainage network controls on debris-flow
860 travel distance along the west coast of the United States, In: The 5th International Conference on Debris-Flow Hazards
Mitigation: Mechanics, Prediction and Assessment, https://doi.org/10.4408/IJEGE.2011-03.B-024, 2011.

Collins, B.D., and Reid, M.E.: Enhanced landslide mobility by basal liquefaction: The 2014 State Route 530 (Oso), Washington,
landslide, GSA Bulletin, 132(3-4), 451-476, https://doi.org/10.1130/B35146.1, 2020.

Corominas, J.: The angle of reach as a mobility index for small and large landslides, Canadian Geotechnical Journal 33(2), 260-
865 271, https://doi.org/10.1139/t96-005, 1996.

Cronkite-Ratcliff, C., Reid, M.E., Brien, D.L., and Perkins, J.P.: Grfin Tools version 1.0: Software package and runtime
documentation, U.S. Geological Survey Software Release, https://doi.org/10.5066/P9NVKFE2, in review.

Crosta, G.B., Cucchiaro, S., and Frattini, P.: Determination of the inundation area for debris flow through semi-empirical
870 equations, In: Mediterranean storms proceedings of the 4th EGS Plinius conference, Spain Universitat de les Illes
  Balears, 2002.

Einbund, M.M., Baxstrom, K.S., and Schulz, W.H.: Map data from landslides triggered by Hurricane Maria in three study areas
  in the Lares Municipality, Puerto Rico, U.S. Geological Survey data release, https://doi.org/10.5066/P9EASZZ7, 2021a.

Einbund, M.M., Baxstrom, K.S., and Schulz, W.H.: Map data from landslides triggered by Hurricane Maria in four study areas in
  the Utuado Municipality, Puerto Rico, U.S. Geological Survey data release, https://doi.org/10.5066/P9ZNUR1P, 2021b.

875 Ellen, S.D., Mark, R.K., Cannon, S.H., and Knifong, D.L.: Map of debris-flow hazard in the Honolulu District of Oahu, Hawaii,
  U.S. Geological survey open-file report 93-213, https://doi.org/10.3133/ofr93213, 1993.

Fan, L., Lehmann, P., McArdell, B., and Or, D.: Linking rainfall-induced landslides with debris flows runout patterns towards
  catchment scale hazard assessment, Geomorphology, 280, 1-15, https://doi.org/10.1016/j.geomorph.2016.10.007, 2017

FLO-2D Software Inc.: FLO-2D user's manual, version 2007.06, 2007.

880 Froude, M.J., and Petley, D.N.: Global fatal landslide occurrence from 2004 to 2016, Natural Hazards and Earth System Sciences
  18(8), 2161-2181, https://doi.org/10.5194/nhess-18-2161-2018, 2018.

Furbish, D.J., and Rice, R.M.: Predicting landslides related to clearcut logging, northwestern California, USA, Mountain
  Research and Development, 3(3), 253-259, https://doi.org/10.2307/3673019, 1983.

George, D.L., and Iverson, R.M.: A depth-averaged debris-flow model that includes the effects of evolving dilatancy, II,
885 Numerical pre-dictions and experimental tests, Proceedings of the Royal Society A: Mathematical, Physical and
  Engineering Sciences, 470(2170), 20130820, https://doi.org/10.1098/rspa.2013.0820, 2014.

Geotechnical Engineering Office, Guidelines on the Assessment of Debris Mobility for Open Hillslope Failure (TGN No. 34),
  Hong Kong, 16 p, 2012.

Gorr, A.N., McGuire, L.A., Youberg, A.M., and Rengers, F.K.: A progressive flow-routing model for rapid assessment of debris-
890 flow inundation, Landslides, 19, 2055–2073, https://doi.org/10.1007/s10346-022-01890-y, 2022.

Griswold, J.P., and Iverson, R.M.: Mobility statistics and automated hazard mapping for debris flows and rock avalanches, U.S.
  Geological Survey Scientific Investigations Report 2007-5276, 59 p. https://doi.org/10.3133/sir20075276, 2008.

Guinau, M., Vilajosana, I., and Vilaplana, J.M.: GIS-based debris flow source and runout susceptibility assessment from DEM
  data – a case study in NW Nicaragua, Nat. Hazards Earth Syst. Sci., 7, 703–716, https://doi.org/10.5194/nhess-7-703-
895 2007, 2007.

Guzzetti, F., Reichenbach, P., Ardizzone, F., Cardinali, M., and Galli, M.: Estimating the quality of landslide susceptibility
  models, Geomorphology 81, 66-184, https://doi.org/10.1016/j.geomorph.2006.04.007, 2006.

Highland, L., and Bobrowsky, P.T.: The landslide handbook: a guide to understanding landslides, Reston, U.S. Geological
  Survey, 2008.

900 Horton, P., Jaboyedoff, M., Rudaz, B., and Zimmermann, M.: Flow-R, a model for susceptibility mapping of debris flows and
  other gravitational hazards at a regional scale, Nat. Hazards Earth Syst. Sci., 13, 869-885. https://doi.org/10.5194/nhess-
  13-869-2013, 2013.

Hsu, K.J.: Catastrophic debris streams (sturzstroms) generated by rockfalls, Geological Society of America Bulletin, 86(1), 129-
  140, https://doi.org/10.1130/0016-7606(1975)86<129:CDSSGB>2.0.CO;2, 1975.

905 Hsu, Y.C., and Liu, K.F.: Combining TRIGRS and DEBRIS-2D models for the simulation of a rainfall infiltration induced
  shallow landslide and subsequent debris flow, Water, 11(5), 890, https://doi.org/10.3390/w11050890, 2019.

Hughes, S.K., Bayouth García, D., Martínez Milian, G.O., Schulz, W.H., and Baum, R.L.: Map of slope-failure locations in Puerto Rico after Hurricane María, U.S. Geological Survey data release, https://doi.org/10.5066/P9BVMD74, 2019.

Hughes, S.K., and Schulz, W.H.: Map depicting susceptibility to landslides triggered by intense rainfall, Puerto Rico. U.S. Geological Survey Open-File Report 2020–1022, 91 p., 1 plate, scale 1:150,000. https://doi.org/10.3133/ofr20201022, 2020.

Hungr, O.J., Corominas, J., and Eberhardt, E.: Estimating landslide motion mechanism, travel distance and velocity, In Landslide risk management, pp. 109-138, CRC Press, 2005.

Hungr, O.J., Evans, S.G., Bovis, M.M., and Hutchinson, J.N.: A review of the classification of landslides of the flow type, Environmental and Engineering Geoscience, 8(3), 221-238, https://doi.org/10.2113/gseegeosci.7.3.221, 2002.

Hungr, O.J., Leroueil, S., and Picarelli, L.: The Varnes classification of landslide types, an update, Landslides, 11(2), 167-194, https://doi.org/10.1007/s10346-013-0436-y, 2014.

Hungr, O.J., Morgan, G.C., and Kellerhals, R.: Quantitative analysis of debris torrent hazards for design of remedial measures, Can. Geotech. J., 21(4), 663-677, https://doi.org/10.1139/t84-073, 1984.

Iverson, R.M.: The physics of debris flows, Reviews of Geophysics, 35(3), 245-296, https://doi.org/10.1029/97RG00426, 1997.

Iverson, R.M., and George, D.L.: A depth-averaged debris-flow model that includes the effects of evolving dilatancy, I, Physical basis, Proceedings of the Royal Society A, Mathematical, Physical and Engineering Sciences, 470(2170), 20130819, https://doi.org/10.1098/rspa.2013.0819, 2014.

Iverson, R.M., George, D.L., Allstadt, K., Reid, M.E., Collins, B.D., Vallance, J.W., Schilling, S.P., Godt, J.W., Cannon, C.M., Magirl, C.S., and Baum, R.L.: Landslide mobility and hazards: implications of the 2014 Oso disaster, Earth and Planetary Science Letters, 412, 197-208, https://doi.org/10.1016/j.epsl.2014.12.020, 2015.

Iverson, R.M., Reid, M.E., Iverson, N.R., LaHusen, R.G., Logan, M., Mann, J.E., and Brien, D.L.: Acute Sensitivity of Landslide Rates to Initial Soil Porosity, Science, 290(5491), 513-516, https://doi.org/10.1126/science.290.5491.513, 2000.

Iverson, R.M., Reid, M.E., Logan, M., LaHusen, R.G., Godt, J.W., and Griswold, J.P.: Positive feedback and momentum growth during debris-flow entrainment of wet bed sediment, Nat. Geosci., 4, 116–121, https://doi.org/10.1038/ngeo1040, 2011.

Iverson, R.M., Schilling, S.P., and Vallance, J.W.: Objective delineation of lahar-inundation hazard zones, Geological Society of America Bulletin, 110(8), 972-984, https://doi.org/10.1130/0016-7606(1998)110<0972:ODOLIH>2.3.CO;2, 1998.

Jibson, R.W.: Debris flows in southern Puerto Rico. Geological Society of America Special Papers, 236, 29-55, https://doi.org/10.1130/SPE236-p29, 1989.

Johnson, A.M.: Physical Processes in Geology: A Method for Interpretation of Natural Phenomena, Freeman Cooper, San Francisco, 1970.

Keellings, D., and Hernández Ayala, J.J.: Extreme rainfall associated with Hurricane Maria over Puerto Rico and its connections to climate variability and change, Geophysical Research Letters, 46, 2964– 2973, https://doi.org/10.1029/2019GL082077, 2019.

Larsen, M.C., and Parks, J.E.: Map showing landslide susceptibility in the Comerío municipality, Puerto Rico, U.S. Geological Survey Open-File Report 98-566, https://doi.org/10.3133/ofr98566, 1998.

Larsen, M.C., and Simon, A.: Rainfall-threshold conditions for landslides in a humid-tropical system, Puerto Rico. Geografiska Annaler, Series A, Physical Geography, 75A 1–2,13–23, https://doi.org/10.2307/521049, 1993.

Larsen, M.C., and Torres-Sanchez, A.J.: The frequency and distribution of recent landslides in three montane tropical regions of Puerto Rico, Geomorphology, 24(4), 309-331, https://doi.org/10.1016/S0169-555X(98)00023-3, 1998.

Legros, F.: The mobility of long-runout landslides, Engineering Geology, 63(3-4), 301-331, https://doi.org/10.1016/S0013-7952(01)00090-4, 2002.

Lepore, C., Kamal, S.A., Shanahan, P., and Bras, R.L.: Rainfall-induced landslide susceptibility zonation of Puerto Rico, Environmental Earth Sciences, 66(6), 1667-1681, https://doi.org/10.1007/s12665-011-0976-1, 2012.

950   Magirl, C.S., Griffiths, P.G., and Webb, R.H.: Analyzing debris flows with the statistically calibrated empirical model LAHARZ in southeastern Arizona, USA, Geomorphology, 119, 111–124, https://doi.org/10.1016/j.geomorph.2010.02.022, 2010.

Major, J.J., Schilling, S.P., Pullinger, C.R., and Demetrio Escobar, C.: Debris-flow hazards at San Salvador, San Vicente, and San Miguel volcanoes, El Salvador, In: Rose WI, Bommer JJ, López DL, Carr MJ, Major JJ (Eds.) Natural Hazards in El Salvador, Geological Society of America Special Paper 375, 89-108, https://doi.org/10.1130/0-8137-2375-2.89,

955   2004.

McDougall, S.: 2014 Canadian Geotechnical Colloquium: Landslide runout analysis—current practice and challenges, Canadian Geotechnical Journal, 54(5), 605-620, https://doi.org/10.1139/cgj-2016-0104, 2017.

McDougall, S., and Hungr, O.: A model for the analysis of rapid landslide motion across three-dimensional terrain, Canadian Geotechnical Journal, 41(6), 1084–1097, https://doi.org/10.1139/t04-052, 2004.

960   Merghadi, A., Yunus, A.P., Dou, J., Whiteley, J., ThaiPham, B., Tien Bui, B., Avtar, R., and Abderrahmane, B.: Machine learning methods for landslide susceptibility studies: A comparative overview of algorithm performance, Earth-Science Reviews 207, 103225, https://doi.org/10.1016/j.earscirev.2020.103225, 2020.

Mergili, M., Marchesini, I., Rossi, M., Guzzetti, F., and Fellin, W.: Spatially distributed three-dimensional slope stability modelling in a raster GIS, Geomorphology, 206, 178-195, https://doi.org/10.1016/j.geomorph.2013.10.008, 2014.

965   Mergili, M., Schwarz, L., and Kociu, A.: Combining release and runout in statistical landslide susceptibility modeling, Landslides 16(11), 2151-2165, https://doi.org/10.1007/s10346-019-01222-7, 2019.

Monroe, W.H.: The karst landforms of Puerto Rico, U.S. Geological Survey Professional Paper 899, https://doi.org/10.3133/pp899, 1976.

Monroe, W.H.: Some tropical landforms of Puerto Rico, U.S. Geological Survey Professional Paper 1159,
970   https://doi.org/10.3133/pp1159, 1980.

Montgomery, D.R., and Dietrich, W.E.: A physically based model for the topographic control on shallow landsliding, Water Resources Research, 30(4), 1153–1171, https://doi.org/10.1029/93WR02979, 1994.

Mudd, S.M., Clubb, F.J., Grieve, S.W.D., Milodowski, D.T., Hurst, M.D., Gailleton, B., and Valters, D.A.: Lsdtopotools2, Zenodo, https://doi.org/10.5281/zenodo.3245041, 2019.

975   Muñoz-Salinas, E., Castillo-Rodríguez, M., Manea, V., Manea, M., and Palacios, D.: Lahar flow simulations using LAHARZ program: Application for the Popocatépetl volcano, Mexico, Journal of Volcanology and Geothermal Research, 182(1-2),13-22, https://doi.org/10.1016/j.jvolgeores.2009.01.030, 2009.

Nicoletti, P.G., and Sorriso-Valvo, M.: Geomorphic Control of the Shape and Mobility of Rock Avalanches, Geological Society of America Bulletin 103, 1365-1373, http://dx.doi.org/10.1130/0016-7606(1991)103<1365:GCOTSA>2.3.CO;2, 1991.

980   Pack, R.T., Tarboton, D.G., and Goodwin, C.N.: SINMAP - A Stability Index Approach to Terrain Stability Hazard Mapping, User's Manual, Produced in ArcView Avenue and C++ for Forest Renewal B.C. under Research Contract No: PA97537-0RE, 1999.

Park, D.W., Lee, S.R., Vasu, N.N., Kang, S.H., and Park, J.Y.: Coupled model for simulation of landslides and debris flows at local scale, Natural Hazards, 81(3), 1653-1682, https://doi.org/10.1007/s11069-016-2150-2, 2016.

985   Pelletier, J.D.: A robust, two-parameter method for the extraction of drainage networks from high-resolution digital elevation
         models (DEMs): Evaluation using synthetic and real-world DEMs, Water Resources Research, 49(1), 75-89.
         https://doi.org/10.1029/2012WR012452, 2013.

       Perron, J.T., Kirchner, J.W., and Dietrich, W.E.: Spectral signatures of characteristic spatial scales and nonfractal structure in
         landscapes, Journal of Geophysical Research, Earth Surface, 113(F4), https://doi.org/10.1029/2007JF0008662, 2008.

990   Pollock, W., Grant, A., Wartman, J., and Abou-Jaoude, G.: Multimodal method for landslide risk analysis, MethodsX, 6, 827-
         836, https://doi.org/10.1016/j.mex.2019.04.012, 2019.

       Powers, D.M.: Evaluation: from precision, recall and F-measure to ROC, informedness, markedness and correlation, J. Mach.
         Learn. Technol., 2011(2), 37–63, https://doi.org/10.48550/arXiv.2010.16061, 2011.

       Quantum Spatial, Inc.: FEMA PR imagery, https://s3.amazonaws.com/fema-capimagery/Others/Maria, last access: October

995   2017.

       Ramos-Scharrón, C.E., Arima, E.Y., Guidry, A., Ruffe, D., and Vest, B.: Sediment mobilization by hurricane-driven shallow
         landsliding in a wet subtropical watershed, Journal of Geophysical Research, Earth Surface, 126(5),
         https://doi.org/10.1029/2020JF006054, 2021.

       Reid, M.E., Brien, D.L., Cronkite-Ratcliff, C., and Perkins, J.P.: Using integrated growth to delineate debris-flow inundation,

1000   E3S Web of Conferences, https://doi.org/10.1051/e3sconf/202341505021, 2023.

       Reid, M.E., Brien, D.L., Cronkite-Ratcliff, C., and Perkins, J.P.: Grfin Tools – Models for portraying landslide and debris-flow
         growth, runout, and inundation, U.S. Geological Survey Techniques and Methods, in review.

       Reid, M.E., Iverson, R.M., Logan, M., Lahusen, R.G., Godt, J.W., and Griswold, J.P.: Entrainment of bed sediment by debris
         flows: results from large-scale experiments, Italian Journal of Engineering Geology and Environment, 367-374,

1005   https://doi.org/10.4408/IJEGE.2011-03.B-042, 2011.

       Reid M.E., Christian S.B., Brien D.L., and Henderson S.: Scoops3D—software to analyze three-dimensional slope stability
         throughout a digital landscape, U.S. Geological Survey Techniques and Methods, book 14, chap. A1, 218 p.,
         https://dx.doi.org/10.3133/tm14A1, 2015.

       Reid, M.E., Coe J.A., and Brien D.L.: Forecasting inundation from debris flows that grow volumetrically during travel, with

1010   application to the Oregon Coast Range, USA, Geomorphology, 273, 396-411,
         http://dx.doi.org/10.1016/j.geomorph.2016.07.039, 2016.

       Reid, M.E., Iverson, R.M., Iverson, N.R., LaHusen, R.G., Brien, D.L., and Logan, M.: Deciphering landslide behavior using
         large-scale flume experiments, In Proceedings of the First World Landslide Forum, The First World Landslide Forum,
         Tokyo, Japan, November 18-21, 2008.

1015   Scheidegger, A.E.: On the prediction of the reach and velocity of catastrophic landslides, Rock Mechanics, 5(4), 231-236,
         https://doi.org/10.1007/BF01301796, 1973.

       Scheip, C., and Wegmann, K.: Insights on the growth and mobility of debris flows from repeat high-resolution lidar, Landslides,
         1-23, https://doi.org/10.1007/s10346-022-01862-2, 2022.

       Schilling, S.P.: Laharz_py—GIS tools for automated mapping of lahar inundation hazard zones, U.S. Geological Survey Open-

1020   File Report 2014-1073, 78 p., https://dx.doi.org/10.3133/ofr20141073, 2014.

       Takahashi, T.: Debris Flow, IAHR Monograph, A. A. Balkema, Rotterdam, 1991.

       Tarboton, D.G.: A new method for the determination of flow directions and upslope areas in grid digital elevation models, Water
         Resources Research, 33(2), 309-319, https://doi.org/10.1029/96WR03137, 1997.

Tarboton, D.G., and Ames, D.P.: Advances in the mapping of flow networks from digital elevation data, In Bridging the Gap:
1025   Meeting the World's Water and Environmental Resources Challenges, 1-10, https://doi.org/10.1061/40569(2001)166,
       2001.

Tarboton, D.G., Dash, P., and Sazib, N.: TauDEM 5.3 Guide to using the TauDEM command line functions,
       http://hydrology.usu.edu/taudem/taudem5/downloads.html, last access: 9 March 2022, 2015.

U.S. Geological Survey: 2015–2016 USGS Puerto Rico LiDAR (project PR_PuertoRico_2015),
1030   https://apps.nationalmap.gov/lidar-explorer/#/, last access: 10 August 2023, 2018.

U.S. Geological Survey: 2018 USGS Puerto Rico – Virgin Islands LiDAR (project PR_PRVI_A_2018),
       https://apps.nationalmap.gov/lidar-explorer/#/, last access: 10 August 2023, 2020a.

U.S. Geological Survey: 2018 USGS Puerto Rico – Virgin Islands LiDAR (project PR_PRVI_D_2018),
       https://apps.nationalmap.gov/lidar-explorer/#/, last access: 10 August 2023, 2020b.

1035 U.S. Geological Survey: 2018 USGS Puerto Rico – Virgin Islands LiDAR (project PR_PRVI_H_2018),
       https://apps.nationalmap.gov/lidar-explorer/#/, last access: 10 August 2023, 2020c.

Wallace, C.S., and Santi, P.M.: Runout Number: a new metric for landslide runout characterization, Environ. Eng. Geosci., 27,
       455–470, https://doi.org/10.2113/eeg-d-20-00144, 2021.

Wallace, C.S., Santi P.M., and Walton, G.: Scoring system to predict landslide runout in the Pacific Northwest, USA, Landslides,
1040   https://doi.org/10.1007/s10346-021-01839-7, 2022.

Zwillinger, D., and Kokoska, S.: CRC Standard Probability and Statistics Tables and Formulae, Chapman and Hall, New York,
       2000, Section 2.2.24.1, 2000.